

This discussion paper is/has been under review for the journal Atmospheric Chemistry and Physics (ACP). Please refer to the corresponding final paper in ACP if available.

**Airborne
measurements of
aerosol optical
properties**

R. Adam de Villiers et al.

Airborne measurements of aerosol optical properties related to early spring transport of mid-latitude sources into the Arctic

R. Adam de Villiers¹, G. Ancellet¹, J. Pelon¹, B. Quennehen²,
A. Scharzenboeck², J. F. Gayet², and K. S. Law¹

¹UPMC Univ. Paris 06, Université Versailles St-Quentin, CNRS/INSU, LATMOS-IPSL, UMR 8190, France

²Laboratoire de Météorologie Physique, Université B. Pascal, CNRS, UMR 6016, France

Received: 1 December 2009 – Accepted: 12 December 2009 – Published: 23 December 2009

Correspondence to: G. Ancellet (gerard.ancellet@upmc.fr)

Published by Copernicus Publications on behalf of the European Geosciences Union.

Title Page

Abstract

Introduction

Conclusions

References

Tables

Figures

◀

▶

◀

▶

Back

Close

Full Screen / Esc

Printer-friendly Version

Interactive Discussion

Abstract

Airborne lidar and in-situ measurements of the aerosol properties were conducted between Svalbard Island and Scandinavia in April 2008. Evidence of aerosol transport from Europe and Asia is given. The analysis of the aerosol optical properties based on a multiwavelength lidar (355, 532, 1064 nm) including depolarization at 355 nm aims at distinguishing the role of the different aerosol sources (Siberian wild fires, Eastern Asia and European anthropogenic emissions). Combining, first aircraft measurements, second FLEXPART simulations with a calculation of the PBL air fraction originating from the three different mid-latitude source regions, and third level-2 CALIPSO data products (i.e. backscatter coefficient, depolarisation and color ratio in aerosol layers) along the transport pathways, appears a valuable approach to identify the role of the different aerosol sources even after a transport time larger than 4 days. Above Asia, CALIPSO data indicate more depolarisation (up to 15%) and largest color ratio (>0.5) for the northeastern Asia emissions (i.e. an expected mixture of Asian pollution and dust), while low depolarisation together with smaller and quasi constant color ratio (≈ 0.3) are observed for the Siberian biomass burning emissions. A similar difference is visible between two layers observed by the aircraft above Scandinavia. The analysis of the time evolution of the aerosol optical properties revealed by CALIPSO between Asia and Scandinavia shows a gradual decrease of the aerosol backscatter, depolarisation ratio and color ratio which suggests the removal of the largest particles in the accumulation mode. A similar study conducted for a European plume has shown aerosol optical properties intermediate between the two Asian sources with color ratio never exceeding 0.4 and moderate depolarisation ratio being always less than 8%, i.e. less aerosol from the accumulation mode.

ACPD

9, 27791–27836, 2009

Airborne measurements of aerosol optical properties

R. Adam de Villiers et al.

Title Page

Abstract

Introduction

Conclusions

References

Tables

Figures

⏪

⏩

◀

▶

Back

Close

Full Screen / Esc

Printer-friendly Version

Interactive Discussion

1 Introduction

Radiative effects of aerosols can be quite different in the Arctic compared to elsewhere (Quinn et al., 2008). Weakly absorbing aerosol layers can be effective for heating the earth-atmosphere system considering the high surface albedo (Pueschel and Kinne, 1995). Frequent haze and cloud layers in the winter-spring period contributes also to surface heating by their infrared emission (Garrett and Zhao, 2006). Cloud formation processes are also very sensitive to the aerosol properties as Arctic clouds often contain low droplet concentrations. Shindell et al. (2008) have examined multi-model results to assess the aerosol and CO transport to the Arctic. They underline in their work the major role played by European and East Asian emissions especially in winter. There is also a very significant altitude dependence of the Arctic sensitivity to emission change. The relative influence of the different mid-latitude aerosol sources was already discussed by Rahn (1981) who concluded using meteorological considerations and observations about the relative importance of the Eurasian transport pathway. The review of Law and Stohl (2007) has also stressed the seasonal change of the air pollution transport into the Arctic with a faster winter circulation implying a stronger influence of the southerly sources. Because of the strong low level winter transport barrier, these emissions are found in the middle and upper troposphere.

Two measurement campaigns in the Arctic took place during the Spring season: TOPSE (Atlas et al., 2003) over the North American sector and ASTAR over the European sector (Engvall et al., 2008). Over the European Arctic sector, the ASTAR results have shown low level of aerosol particles even in layers with elevated CO, suggesting aerosol removal in clouds. Occurrence of layers of non volatile and aged aerosol however increases with altitude in this region. The conditions during the ASTAR-2007 experiment were however exceptionally clean and other studies show events with large amount of polluted air masses in the lower troposphere, e.g. in spring 2006 (Stohl et al., 2007a).

**Airborne
measurements of
aerosol optical
properties**

R. Adam de Villiers et al.

Title Page

Abstract

Introduction

Conclusions

References

Tables

Figures



Back

Close

Full Screen / Esc

Printer-friendly Version

Interactive Discussion

**Airborne
measurements of
aerosol optical
properties**

R. Adam de Villiers et al.

[Title Page](#)[Abstract](#)[Introduction](#)[Conclusions](#)[References](#)[Tables](#)[Figures](#)[⏪](#)[⏩](#)[◀](#)[▶](#)[Back](#)[Close](#)[Full Screen / Esc](#)[Printer-friendly Version](#)[Interactive Discussion](#)

long range transport of the aerosol plumes from the source regions.

2 Aircraft data and meteorological context

2.1 Flight description and meteorological context

On 11 April 2008, the ATR-42 flew from Kiruna (68° N, 20° E) to the latitude circle at 73° N. The purpose of this flight was to sample two kinds of air masses: one transported across the North Pole to Northern Scandinavia and the other one exported from Europe by mid-latitude weather systems. The Lagrangian FLEXPART model used in a forecast mode (Stohl et al., 2004) indeed showed a well defined CO plume at 72° N and suggested long range transport of mid-latitude emissions. The meteorological situation can be described using the 850 hPa map of the equivalent potential temperature (θ_e) and the vertical cross section of the specific humidity at 20° E along the flight pattern (Fig. 1). It shows that the aircraft measurements took place between two frontal zones at 68° N and 74° N. Subsidence of dryer air from the mid-troposphere occurred in this region where the 290–300 K isentropic surfaces are tilted. The wind field at 700 hPa indicates a weak southerly flow in the southern part of the domain but then a well defined northerly flow at latitudes higher than 70° N (Fig. 2). We can also notice that, further East at 30° E, the flow at northern latitudes remains southerly and intensifies. The corresponding flow curvature is related to the positive vorticity anomaly located at 25° E south of the Spitzbergen Island. A flight in the latitude band 68°–72° N is then interesting as its southern section characterizes an upward and northward flow corresponding to a fast and direct export from Europe, while its northern section samples the downward branch of the Arctic outflow with aged mid-latitude emissions according to the FLEXPART forecast. The red solid line in Fig. 11 corresponds to the aircraft vertical profile. During the first part of the flight between 10:00 UT and 11:30 UT, the aircraft flew above 3 km before a descent to explore the Arctic planetary boundary layer (PBL) at 72.5° N. During the second part of the flight, i.e. the return to Kiruna, the air-

Airborne measurements of aerosol optical properties

R. Adam de Villiers et al.

Title Page

Abstract

Introduction

Conclusions

References

Tables

Figures

⏪

⏩

◀

▶

Back

Close

Full Screen / Esc

Printer-friendly Version

Interactive Discussion

craft stayed within the PBL for aerosol-cloud interaction studies and made a second exploration of the free troposphere for latitude below 70.5° N. So in addition to lidar data below the aircraft, four complete vertical profiles of the aerosol concentrations are derived from the in-situ measurements between 0 and 5500 m.

2.2 Lidar measurements

A backscatter lidar provided measurements of total attenuated backscatter vertical profiles at three wavelengths: 355, 532 and 1064 nm. An additional channel recorded the perpendicular attenuated backscatter vertical profile at 355 nm. The lidar characteristics are summarized in Table 1. A vertical cross section of the total attenuated backscatter in the IR channel is shown in Fig. 3. The areas with very large backscatter in the altitude range 1–2 km correspond to cloud layers developing at the top of the Planetary Boundary Layer (PBL). The cloud top reaches 3 km as the aircraft approaches the Arctic front. In the cloud free area, the layer from 0 to 1 km with larger aerosol backscatter values correspond to the PBL. Well defined layers with enhanced aerosol backscatter are also detected in the free troposphere. The layer with a depth less than 1 km and with a meridional extent between 70° N and 72.5° N has the strongest relative signal compared to the background aerosol in the IR. This layer has also a slight vertical tilt, probably corresponding to the tilt of the isentropic surface. Another aerosol plume is also seen at latitudes less than 69.2° N, but with a much larger altitude range between 3.5 and 5.5 km and weaker backscatter at 1064 nm.

To further characterize these two layers, four 20-s averages of lidar profiles are analyzed: the first one corresponds to the thick layer at 68.9° N (named layer I hereafter), the second and third ones are through the longest and thin layer at 69.6° N and 71.6° N (layer II-A and II-B) and the last one at 70.4° N samples the cloud free marine PBL over the Arctic ocean. The attenuated backscatter ratio, $R(z)$, is defined in this paper as the Rayleigh normalized total volume backscatter, only attenuated by the aerosol extinction (see Annexe I). It is calculated for the 4 selected averages as a function of the altitude z , using an instrument calibration factor. This factor is calculated using areas

Airborne measurements of aerosol optical properties

R. Adam de Villiers et al.

Title Page

Abstract

Introduction

Conclusions

References

Tables

Figures

⏪

⏩

◀

▶

Back

Close

Full Screen / Esc

Printer-friendly Version

Interactive Discussion



**Airborne
measurements of
aerosol optical
properties**

R. Adam de Villiers et al.

Title Page

Abstract

Introduction

Conclusions

References

Tables

Figures

⏪

⏩

◀

▶

Back

Close

Full Screen / Esc

Printer-friendly Version

Interactive Discussion

with mainly Rayleigh contribution to the IR lidar signal in the altitude range close to the aircraft (e.g. at 69.6° N above 5 km or at 70.3° N near 3 km). This is done independently for each wavelength and the consistency of the calibration factor is checked using different aerosol free areas whenever possible. This is the major source of error in the calculation of $R(z)$, and the uncertainty was assumed to be less than 10% at 532 nm and 355 nm, less than 20% at 1064 nm. The latter was derived from a sensitivity study using different possible calibration factors and different flight analysis.

The 355-nm pseudo depolarization ratio, δ_{355} , is calculated together with the pseudo color ratio, as a mean to identify aerosol type (Cattrall et al., 2005) (see Appendix A for the definitions of these parameters). The pseudo depolarization ratio is calibrated on molecular scattering with an error estimated to be 20%. The depolarization and color ratios are also measured by the CALIOP space-borne lidar and will be used to compare the features observed by the two instruments. The CALIOP pseudo depolarisation ratio is however given at 532-nm and one will have to account for the spectral variation of this ratio from 355 nm to 532 nm when comparing aircraft and satellite observations (Freudenthaler et al., 2009; Sugimoto and Lee, 2006).

The $R(z)$ vertical profiles for each wavelength and the 4 selected latitudes are given in Fig. 4. For the strongest aerosol layer at 69.7° N (layer II-A), the R increase is present in the three wavelength channels. The maximum R value at 532 nm is of the order of 2 and it corresponds to a 532-nm aerosol backscatter coefficient of the order of $10^{-3} \text{ km}^{-1} \text{ sr}^{-1}$ and therefore a small optical depth for layer II-A ($\approx 3\text{--}4 \times 10^{-2}$) assuming a 532-nm lidar ratio of the order of 70 sr (Cattrall et al., 2005), i.e. considering for example biomass burning aerosol. For the other layers (I and II-B), R is of the order of 2 at 1064 nm and between 1.3–1.4 at 532 nm. Layers with IR values of R less than 1.5 will not be considered in the following discussion.

The pseudo depolarization ratios δ_{355} are shown for the four profiles (Fig. 5a) and it becomes larger than the molecular depolarization only for the layer II-A at 69.7° N near 3.2 km where it is of the order of 0.019. Notice that it is also larger than the Rayleigh depolarisation in the Arctic PBL. For the layer II-A, the aerosol depolarisation

ratio, corresponding to a δ_{355} of 0.019, is of the order of 3%, i.e. a value close to pure molecular depolarization and much smaller than the 532-nm aerosol depolarisation ratio reported by Gobbi et al. (2003) for a mountain site in Italy. This would be consistent with a significant fraction of spherical aerosol even though we are able to detect some depolarisation in layer II-A.

The pseudo color ratio plot for the four profiles shows also largest values (0.13 ± 0.009) in layer II-A at 69.6° N (Fig. 5b). The smaller values (0.08 ± 0.01) in the southern layer are consistent with the hypothesis of smaller aerosol size in layer I. The color ratio in layer II-B at 71.6° N near 3.5 km (0.10 ± 0.01) is intermediate between the two previous cases. The main characteristics of the aerosol layers identified in Fig. 4 are listed in Table 2 with the expected uncertainty on the color and depolarisation ratio. The aerosol color ratio, which is proportionnal to $(R_{1.06} - 1)/(R_{0.53} - 1)$, is also listed in Table 2 as it is more directly linked to the aerosol backscatter wavelength dependency (see Appendix A).

For all the layers, pseudo color ratios are much smaller than the reported values of Catrall et al. (2005), which are greater than 0.4. In the work of Catrall et al. (2005), the color ratios are calculated using data from the AERONET photometer network, where much larger aerosol optical depths (>0.1) are considered. For our smaller aerosol optical depths, the pseudo color ratio increase could remain below 0.2 when the fraction of coarse aerosol remains small enough and the 532-nm Angstrom coefficient is ≥ 2 (see Appendix A). In Table 2 the aerosol color ratio is always around 0.2 for all the layers and the variability from one layer to the next is smaller than the large error on this ratio. The pseudo color ratio is however showing a significant variability especially for layer II-A. Since this pseudo ratio can be used for deriving the variability of the aerosol size when all the layers exhibit similar R values, one will rely mainly on this parameter to discuss differences in the layer optical properties (see Appendix A). The results of Table 2 show that the apparently homogeneous layer II is likely to be formed of several aerosol sources since layer II-A and II-B have different optical characteristics.

Airborne measurements of aerosol optical properties

R. Adam de Villiers et al.

[Title Page](#)[Abstract](#)[Introduction](#)[Conclusions](#)[References](#)[Tables](#)[Figures](#)[⏪](#)[⏩](#)[◀](#)[▶](#)[Back](#)[Close](#)[Full Screen / Esc](#)[Printer-friendly Version](#)[Interactive Discussion](#)

To summarize, the airborne lidar data show that:

- two layers (I and II) are detected with markedly different vertical structure and backscatter values implying different aerosol sources and probably different transport processes
- layer I has low depolarization and lowest color ratio related to a very small fraction of coarse size particles
- layer II is not homogeneous with, according to the color ratio values, larger particles than layer I and even some depolarization in layer II-A.

To get more insight in the airborne lidar data interpretation, we have taken advantage of the flight pattern to include also the analysis of the in-situ measurements when the aircraft has crossed the layers observed by the lidar.

2.3 In-situ measurements

Ozone and carbon monoxide (CO) have been measured on the ATR-42. The CO is especially useful as it can indicate if an air mass has been influenced by combustion processes less than 10–20 days before. Regarding the aerosol concentrations, an optical counter (CPC-3010) measured the number of submicronic particles with sizes larger than 10 nm and a Passive Cavity Aerosol Spectrometer Probe (PCASP SPP-200) provided the number of particles in 30 size bins between 0.1–3 μm . In this paper the PCASP data are summed over all the size bins to get a concentration number comparable to the optical counter. The differences between the two numbers will be mostly related to a large fraction of small particles (<100 nm) detected by the optical counter but not seen by the PCASP.

The CO and the aerosol concentrations from the PCASP and the CPC are shown in Fig. 6 for latitudes, respectively less and greater than 70° N, the second plot corresponding to the numerous crossing of the layer II identified by the lidar. The carbon monoxide variability is generally well correlated with the aerosol concentrations. The

Airborne measurements of aerosol optical properties

R. Adam de Villiers et al.

Title Page

Abstract

Introduction

Conclusions

References

Tables

Figures

⏪

⏩

◀

▶

Back

Close

Full Screen / Esc

Printer-friendly Version

Interactive Discussion



CO variability is of the order of 100 ppb and it is not very different for the southerly flow and the Arctic outflow. This variability can be explained by the highly stratified aerosol and chemical composition of the free troposphere as shown by the lidar. The smallest CO values around 130 ppb correspond to the cleanest and oldest air masses.

When comparing the PCASP and the optical counter data, one can notice higher concentrations of small particles in the southern section of the flight. This is related to either the removal of larger particles during the transport from mid-latitudes or to the generation of new smaller particles. The two hypotheses imply anyway differences for layer I and II in the air mass age since exposure to emissions or in the nature of the emissions (e.g. more SO₂ concentrations (Weber et al., 2003) or more organic emissions from continental regions over Northern Europe (Sellegrì et al., 2005)). A more direct way to demonstrate the larger fraction of very small particles is to plot the size spectrum measured along the flight by a Scanning Mobility Particle Sizer (SMPS) for particle smaller than 300 nm and the PCASP for larger particles (Fig. 7). It shows indeed smaller particle sizes (30–200 nm) for the southern section of the flight, while the Arctic outflow corresponds to larger particles (100–300 nm). This is consistent with the interpretation of the differences between the PCASP and the optical counter. It is also noticeable that the fraction of particles with a diameter exceeding 300 nm are increasing in the layer II-A at 69.6° N, i.e. where the pseudo color and depolarization ratio are maximum in the lidar data.

The analysis of the in-situ data is quite useful to shed light on interpretation of the lidar data and we can say that:

- the lidar aerosol layers are mostly related to either biomass burning or urban/industrial sources considering the good correlation between aerosol and CO concentration
- the pseudo color ratio analysis is consistent with the observed aerosol size distribution showing the largest aerosol size for the layer II-A, even though the aerosol optical depth is small and the variability of this ratio is weak.

**Airborne
measurements of
aerosol optical
properties**

R. Adam de Villiers et al.

Title Page

Abstract

Introduction

Conclusions

References

Tables

Figures

⏪

⏩

◀

▶

Back

Close

Full Screen / Esc

Printer-friendly Version

Interactive Discussion



To understand the respective influence of the aging and the nature of the sources, one can have a look now at the modeling of the air mass transport.

3 Modeling of the transport to the Arctic

3.1 Description of the FLEXPART simulations

5 The origin of the observed air masses was studied using the Lagrangian Particle Dispersion Model (LPDM) FLEXPART version 6 (Stohl et al., 1998, 2002) driven by 6-hourly ECMWF analyses (T213L91) interleaved with operational forecasts every 3 h. In addition to classical advection, the LPDM includes turbulent diffusion, parameterizations of sub-grid scale convection and of topographic processes, as well as online
10 computation of potential vorticity (PV) for each air parcel. The fraction of particles with $PV > 2$ PVU ($1 \text{ PVU} = 10^{-6} \text{ K kg}^{-1} \text{ m}^2$) is calculated as a function of time to estimate the probability of transport from or into the stratosphere. Previous studies have shown that a fraction larger than 20% corresponds to a significant influence of the stratosphere-troposphere exchange (STE) processes. We modified the FLEXPART model to intro-
15 duce the calculation of the fraction of particles originating below an altitude of 3 km, for three areas corresponding to different emissions of particulate matter and CO: Europe (latitude $< 55^\circ \text{ N}$, longitude $\in [-10^\circ \text{ W } 30^\circ \text{ E}]$), Asia (latitude $< 55^\circ \text{ N}$, longitude $\in [30^\circ \text{ E } 180^\circ \text{ E}]$), North America (latitude $< 55^\circ \text{ N}$, longitude $\in [-180^\circ \text{ W } -30^\circ \text{ W}]$).

Next we have divided the lidar vertical cross-section of Fig. 3 in 130 boxes with
20 the following size: depth of 500 m and horizontal size of $0.5^\circ \times 0.5^\circ$. For each box, 2000 particles were released during 60 min and the dispersion computed for 7 days backward in time. As we focus on layers, our aim is to document their history as long as they remain coherent, i.e. before they undergo strong mixing which, as reported by Methven et al. (2006), becomes significant after 4 days for trajectories arriving above
25 Western Europe. The vertical cross-section of the air mass origin can be reconstructed using a plot of the fraction of particles being in the lower troposphere of a given region

Airborne measurements of aerosol optical properties

R. Adam de Villiers et al.

Title Page

Abstract

Introduction

Conclusions

References

Tables

Figures

⏪

⏩

◀

▶

Back

Close

Full Screen / Esc

Printer-friendly Version

Interactive Discussion



5 days before the lidar observations (Fig. 8). The comparison of the cross-sections for different transport time has shown that the 4 to 6 days cross sections provide the best well defined layering comparable to the observations.

The transport pathway for the ensemble of 2000 particles released in a given box can also be described by the position every 24 h of 5 clusters identified among the particle plume. Two examples are given in Fig. 9 for a box in the southern section of the flight mainly influenced by the European emissions and a box in the northern section where air masses are coming from Asia. The size of the clusters corresponds to the number of particles included in the cluster and the color to its altitude. The color of the mean trajectory of the particles is the altitude of the ending point. If the layer remains coherent the five clusters (or at least the largest ones) stay close to each other. Often the dispersion of the clusters is too large after 4–5 days to identify a direct link with a single source region or to be able to establish a Lagrangian connection between two different observations.

3.2 Air mass origins and CALIPSO overpasses

The cross-section in Fig. 8 nicely shows that the measurement area between 3.5 and 5 km in the southern section ($<70^\circ$ N) is mainly related to European emissions with a fraction of particles larger than 30% coming from the European PBL. The area corresponding to the largest lidar signal comes from Central Europe with a significant upward motion from the PBL (altitude <2 km) to the 4-km altitude range above Denmark (Fig. 9a). This took place 3.5 days because of the combined action of two low pressure systems: one over the North Sea and the other one over the Western Mediterranean Sea. Central European emissions first transported by the cold conveyor belt of the southernmost low were then further uplifted in the warm conveyor belt of the northernmost low.

The aerosol layer observed in the northern section of the flight is transported from Asia as shown by the cross-section of the Asian fraction where boxes with fraction

**Airborne
measurements of
aerosol optical
properties**

R. Adam de Villiers et al.

Title Page

Abstract

Introduction

Conclusions

References

Tables

Figures

⏪

⏩

◀

▶

Back

Close

Full Screen / Esc

Printer-friendly Version

Interactive Discussion

larger than 30% matches exactly the sawtooth motion of the aircraft between 70.5° N and 72.5° N. An example of a trajectory for the box at 72° N, 3.7 km (Fig. 9b) shows that the upward motion took place in a frontal system developing above North Eastern China from 5 April to 7 April (see the θ_e map showing the position of the low level front and the advection of warm and humid air mass toward the Arctic in Fig. 10).

The influence of STE below 6 km remains negligible (the PV fraction in the FLEX-PART runs are always less than 10%) and the clean region of the lidar section above 3.5 km between 69.5° N and 70° N remains influenced by the European emission but uplifting is mainly driven by the 7 April low pressure over the North Sea. The dominant European sources are then from the southern coast of the Baltic Sea, where less CO emissions are expected and aerosol probably have been washed out in the northern part of the warm conveyor where heavy precipitations are generally encountered at low level (Bethan et al., 1996).

To be more specific about the geographical extent of the Asian and European sources responsible for the aerosol and CO increase, we have also used the map of the potential emission sensitivity (PES) described in Seibert and Frank (2004) and calculated for different positions along the aircraft track by John Burkhardt for the POLARCAT project (web site <http://transport.nilu.no/flexpart-projects>). The PES is shown in Fig. 11 for 4 different latitudes along the flight cross-section: 68.6° N (European plume), 70.2° N, 72° N, 72.4° N (Asian plume). The 72.4° N and 72° N air masses correspond to, respectively the aerosol layer at 5 km and at 3.7 km in the northernmost part of the lidar cross-section. We can see that the European emissions related to our observations are mainly from Eastern Europe and that the air mass lifetime is of the order of 4–5 days. For the Asian plume, we can see that it cannot be regarded as a single layer with a similar history but most likely to two different plumes: one is related to the fire emissions which took place in April 2008 over Siberia (see the 10-day mean fire map plot measured by MODIS from 31 March 2008 to 9 April 2008 in Fig. 12) east of the Baïkal lake and the other one is related to the anthropogenic emissions from North Eastern Asia (Streets and Waldhoff, 2000). The strong impact of the spring

Airborne measurements of aerosol optical properties

R. Adam de Villiers et al.

Title Page

Abstract

Introduction

Conclusions

References

Tables

Figures

⏪

⏩

◀

▶

Back

Close

Full Screen / Esc

Printer-friendly Version

Interactive Discussion

2008 Siberian fires on the atmospheric composition have been already observed over Alaska (Warneke et al., 2009) and by the satellite observations (Coheur et al., 2009).

Using air mass trajectory estimates similar to the results shown in Fig. 9, one can look for the CALIPSO satellite tracks related to our observations with the aircraft. This was done for three groups of trajectories corresponding to the boxes of Fig. 8 which are within the black rectangles indicated in this figure: (i) the first area near 69° N (six trajectories) matches the European plume (layer I in the lidar data), (ii) the second one at 4 km near 70.5° N (six trajectories) matches the southern part of the Asian plume (layer II-A) and (iii) the last rectangle at 4 km near 72° N (4 trajectories) corresponds to the northern part of the Asian plume (layer II-B). A CALIPSO track was selected if the time and horizontal position of the satellite overpass was less than, respectively 2 h and 200 km, from the air mass positions in the FLEXPART runs. The track sections (line) and the FLEXPART air mass positions (stars) are shown in Fig. 13 where the color scale corresponds to the elapsed time between the CALIPSO observations and the aircraft observations. One can see that the evolution of the aerosol content of the 3 selected groups can be analysed for a 6 day period for the Asian plume and a 4 day period for the European plume, i.e. the time corresponding to the transport from the source region. The selected CALIPSO observations are coming from the same source region for group (ii) and (iii) but the pathways are slightly different. The air masses and the corresponding CALIPSO observations remain over the continent with the northward transport near 135° E three days before for group (iii), i.e. the northern section of the plume. The group (ii) shows a longer pathway with the northward transport more often over the Pacific ocean and even toward Alaska before coming back west to Scandinavia. Several CALIPSO overpasses are indeed above Alaska for group (ii).

Even though there are different pathways for group (ii) and (iii), we will not distinguish the two groups any further as their air masses are both connected to the position of the Siberian fires and North Eastern Asia emissions. The distinction of the CALIPSO aerosol layers related to these two sources will have to be deduced from the actual latitude/longitude of the detected layers in the CALIPSO observations.

Airborne measurements of aerosol optical properties

R. Adam de Villiers et al.

[Title Page](#)[Abstract](#)[Introduction](#)[Conclusions](#)[References](#)[Tables](#)[Figures](#)[⏪](#)[⏩](#)[◀](#)[▶](#)[Back](#)[Close](#)[Full Screen / Esc](#)[Printer-friendly Version](#)[Interactive Discussion](#)

Notice that there is a likely Lagrangian connection between aircraft observations made in Alaska between 4 and 7 April and the lidar observations of group (ii). This will be studied in a future paper using a Lagrangian model for aerosol aging.

4 Optical properties of the aerosol plumes

5 The level-2 CALIOP aerosol data products have been analysed along the selected CALIPSO track using the 5-km horizontal average profiles (Liu et al., 2009). We have considered the aerosol layer properties when the aerosol layer altitude is less than 1 km away from the air mass altitudes calculated by FLEXPART. Two additional conditions are: a minimum horizontal averaging of 80 km and a 532-nm layer optical depth $>3\%$.

10 The last two conditions are necessary considering the limited aerosol optical depth of layer revealed by the airborne lidar observations. For a given CALIPSO track, the average position of all the nearby FLEXPART air masses is calculated and the track is analysed over a ± 300 km distance around this average position. The mean 532-nm attenuated backscatter, the color ratio and the 532-nm depolarization ratio are reported

15 for all the layers which fulfilled the previous conditions in Table 3 for the FLEXPART trajectories of group (ii) and (iii) and in Table 4 for the group (i). The comparison between the CALIPSO tracks in Fig. 13 and the time and position of the detected layers show that 65% and 50% of the CALIOP data exhibit aerosol layers with optical depths >0.03 for the Asian plumes (Table 3) and the European plume (Table 4), respectively.

20 We can notice that the uncertainties in the color ratio and the depolarisation ratio are often very large and cannot be used for a truly quantitative analysis of the aerosol composition and evolution. The largest possible ratios (i.e. the mean+the standard deviation) still contains a meaningful indication about the possible source and the rough evolution of the optical properties (see (Omar et al., 2009) for interpretation of the color ratio and the depolarisation ratio for aerosol classification).

25

The analysis of the two tables shows that the CALIPSO layers detected in the region $65\text{--}85^\circ$ N, $10\text{--}30^\circ$ E (i.e. in the vicinity of the measurement zone) exhibit moderate 532-

Airborne measurements of aerosol optical properties

R. Adam de Villiers et al.

Title Page

Abstract

Introduction

Conclusions

References

Tables

Figures

◀

▶

◀

▶

Back

Close

Full Screen / Esc

Printer-friendly Version

Interactive Discussion

nm backscatter values, low color ratio (≤ 0.25) and almost no depolarisation ($\approx 3\%$). This is consistent with the properties of the layers measured by the aircraft (Table 2). The depolarisation values measured at 355 nm by the aircraft (2%) are slightly smaller than the expected δ_{355} (2.5%) for a δ_{532} of 3%, but the CALIPSO depolarisation values are nevertheless smallest in this region. The good correspondence between the aerosol properties of the CALIPSO layers and the airborne lidar layers for a time scale of 1 day, is the first necessary condition if one aims at using the CALIPSO observations further upwind of the region studied by the aircraft.

The analysis of Table 3 has been done focussing on layers with backscatter values, $\beta_{532} \geq 2 \times 10^{-3} \text{ km}^{-1} \text{ sr}^{-1}$ i.e. with an intensity strong enough to be able to discuss the optical properties. The position of the layers must also be considered in the interpretation of this table as three Asian sources are known to dominate the aerosol composition at this time of the year: the desert dust advected from the Gobi and Taklamakan desert (Duce et al., 1980) in the latitude band $40^\circ \text{ N} - 50^\circ \text{ N}$, the industrial emissions from the Heilongjiang region further east in the same latitude band, and the forest fires from the Baikal lake region in the latitude band $50^\circ \text{ N} - 55^\circ \text{ N}$. Therefore three main results can be underlined from this table:

- Looking at the strongest aerosol layers prior to 8 April, two kinds of aerosol properties can be found in the $45^\circ - 52^\circ \text{ N}$ where several sources influence the aerosol properties: one with low color ratio (near 0.3) and low δ_{532} (0–5%) for longitude $< 125^\circ \text{ E}$, and the other one with larger color ratio (0.5 to 1) and larger δ_{532} (10–14%) for longitude $> 135^\circ \text{ E}$ (i.e. near the Pacific coast).
- Near the Siberian sources ($55^\circ - 60^\circ \text{ N}$, $90^\circ - 120^\circ \text{ E}$), $\beta_{532} \leq 2 \times 10^{-3} \text{ km}^{-1} \text{ sr}^{-1}$ with a 0.3 color ratio and low δ_{532} (0–5%), i.e. with probably small aerosol which did not have time to grow as when transported through a very humid frontal system.
- At latitude larger than 60° N (i.e. in the Arctic region), one can distinguish two regions: (i) the layers detected above Alaska with a color ratio of 0.3–0.4 and some depolarization (9–10%) although smaller than the values for lower latitudes

27806

**Airborne
measurements of
aerosol optical
properties**

R. Adam de Villiers et al.

Title Page

Abstract

Introduction

Conclusions

References

Tables

Figures

◀

▶

◀

▶

Back

Close

Full Screen / Esc

Printer-friendly Version

Interactive Discussion



Airborne measurements of aerosol optical properties

R. Adam de Villiers et al.

Title Page

Abstract

Introduction

Conclusions

References

Tables

Figures



Back

Close

Full Screen / Esc

Printer-friendly Version

Interactive Discussion



near the Asian Pacific coast, (ii) the layers in the Eurasian Arctic with a variable color ratio 0.3–0.5 and lower δ_{532} (2–8%).

- As the air masses are transported from Asia to Scandinavia across the Arctic, there is a general tendency for decreasing β_{532} from 3 to $1.5 \times 10^{-3} \text{ km}^{-1} \text{ sr}^{-1}$ and fewer air masses with elevated pseudo color ratio or pseudo depolarisation ratio. Notice also that there is not a very clear dependency of the optical properties with altitude in the detected layers considered in this study.

One plausible hypothesis for explaining the largest δ_{532} and elevated color ratio for the CALIPSO layers in the area (45° – 52° N, 135° – 140° E) is that the southernmost CALIPSO tracks near the coast are influenced both by the desert dust and North Eastern Asia emissions. The more elevated color ratio is consistent with larger aerosol particles resulting from a remaining influence of dust but also from the likely growth of the pollution aerosol in the frontal system responsible for the northward transport which develops near the Pacific coast on 5–7 April (Fig. 10). Airborne in-situ aerosol measurements of the ratio of ultrafine (3–70 nm) to fine particles (70–200 nm) over Siberia in Spring 2006 by Paris et al. (2009) have shown, for similar meteorological conditions, that this ratio decreases for polluted air masses from North Eastern Asia.

Further west the northward motion being less efficient, the Siberian fires gradually become the main aerosol sources, explaining a significant decrease in both the color ratio and δ_{532} , as expected for biomass burning aerosol according to the work of Cattrall et al. (2005). This means that the three sources have influenced the aerosol composition over Scandinavia and that the depolarization ratio should provide a way to separate the biomass burning plume from the North Eastern Asia emissions because of the remaining influence of the desert emissions in the 40° N– 50° N latitude band.

Above 60° N the Alaskan layers can be considered as aged Asian layer being transported across the Pacific to Alaska as reported in the analysis of the 2008 Spring period transport pathways described in Fuelberg et al. (2009), but also from the modeling work of Fisher et al. (2009) showing the widespread influence Asian CO sources

including Alaska. This can explain the values of the depolarization ratio which are intermediate between the low values above Scandinavia and the large values above North Eastern Asia. Considering all the layers in the Arctic region the slight decrease of the color ratio which is concomitant with the lower β_{532} , would indicate the gradual removal of the largest aerosol particles due either to mixing of the different aerosol type being present above Asia or to the wet removal of the largest hydrophilic aerosol particles during the transport processes.

Finally the CALIPSO analysis of the aerosol layer properties above Asia would now suggest that the source attribution of the different layers observed by the lidar in the Asian plume could be the following: remaining influence of North Eastern Asia emissions mixed with dust for the layer II-A at 69.7° N and more predominantly Siberian fire influence for the layer II-B further north. The unique use of the FLEXPART simulations would be weaker to derive such a conclusion considering the uncertainties for distinguishing sources of nearby layers when the transport time is longer than 5 days.

When it is compared with the analysis of the Asian plume, the results of Table 4 show smaller changes of the aerosol properties during the transport from Central Europe. The color ratio and the depolarisation ratio are less than, respectively 0.4 and 8% above the sources in Central Europe, i.e. intermediate between the ones observed for the two type of Asian layers previously discussed. It is not so surprising since the industrial european emissions dominate the aerosol composition where larger aerosols from the accumulation modes are less numerous. Episodic transport from the Sahara in the exported air mass from Europe may exist (Hamonou et al., 1999). Fuelberg et al. (2009) shows however that 10-day trajectories reaching 70° N and originating from Sahara are almost negligible during the 2008 Spring season compared to the potential export of dust from Asian desert.

Airborne measurements of aerosol optical properties

R. Adam de Villiers et al.

Title Page

Abstract

Introduction

Conclusions

References

Tables

Figures

⏪

⏩

◀

▶

Back

Close

Full Screen / Esc

Printer-friendly Version

Interactive Discussion

5 Conclusions

In this paper we have analysed aerosol airborne and spaceborne lidar data related to the transport of two different sources into the Arctic: a European plume and an Asian plume. Both plumes exhibit elevated CO concentrations indicating a significant fraction of either biomass burning or anthropogenic pollution sources. Although the aerosol optical depths are similar for both layers, their optical properties are quite different. In this work, we have used mainly the pseudo depolarisation and color ratio to distinguish both layers. The European plume contains smaller particles with very low depolarization ($1.3\pm 0.3\%$) and low color ratio ($0.9\pm 1\%$). The Asian plume is characterized by larger particles and some depolarisation ($2\pm 0.2\%$) in one layer (i.e. with a larger fraction of dust particles). Measurements of the aerosol size spectrum along the flight have also shown that the variability of the color ratio can be related to the actual change of the aerosol size distribution even for layers where the optical depth is small and consequently an increase of the color ratio error. This gives some confidence in the possibility of using the CALIPSO data, which provides similar aerosol optical characteristics, in the analysis of the aerosol layers transported across the Arctic. The study of the transport of the air masses where lidar data are available, is done with specific FLEXPART simulations where we have included a calculation of the PBL air fraction originating from three different mid-latitude source regions: Asia, North America and Europe. The combination of CALIPSO observations and FLEXPART simulations improves the identification of the aerosol sources and the discussion of the temporal evolution of the aerosol optical characteristics. For example in the case of the Asian plume, the CALIPSO data provide a mean to distinguish the aerosol layer properties near the sources, which were then related to similar differences in the aerosol layers observed by the aircraft after a transport time of more than 4 days. Above Asia, the CALIPSO data indeed suggest more depolarisation (up to 15%) and the largest color ratio (>0.5) for North Eastern Asia emissions where there is a mixture of Asian pollution and dust, while low depolarisation together with smaller and quasi constant

Airborne measurements of aerosol optical properties

R. Adam de Villiers et al.

Title Page

Abstract

Introduction

Conclusions

References

Tables

Figures

⏪

⏩

◀

▶

Back

Close

Full Screen / Esc

Printer-friendly Version

Interactive Discussion

color ratio (≈ 0.3) are observed for the Siberian biomass burning emissions. A similar difference is visible between layer II-A and II-B observed by the aircraft above Scandinavia. It means that the three aerosol sources (biomass burning, industrial emissions and desert) are still visible after being transported across the Arctic, the influence of the mixture of Asian pollution and dust being stronger for layer II-A. Of course the analysis remains qualitative considering the difficulty to quantify the different processes modifying the aerosol properties. This would require specific Lagrangian modeling of the aerosol evolution which is not within the scope of this paper. Notice however that it would have been hard to discuss the remaining influence of different aerosol sources using the trajectory model alone which become less able to distinguish nearby sources after several days of transport.

The analysis of the time evolution of the aerosol optical properties revealed by CALIPSO between the source regions and Scandinavia after 4 days of transport over the Arctic, suggests a gradual decrease in the aerosol backscatter, the depolarisation ratio and the color ratio which can be related to the removal of the largest particles in the accumulation mode (e.g. by wet removal in the frontal system responsible for the northward transport). A mixture of the three Asian aerosol sources will also participate to reduce the depolarization and color ratio towards their lowest values, respectively 0.1 and 2%.

Finally, a similar study conducted for a European plume has shown aerosol optical properties intermediate between the two Asian sources with color ratio never exceeding 0.4 and moderate depolarisation ratio being always less than 8%, i.e. less aerosol from the accumulation mode. As for the Asian plume, the time evolution suggests the removal of the largest particles, explaining the aerosol spectrum observed by the aircraft in the European plume.

**Airborne
measurements of
aerosol optical
properties**

R. Adam de Villiers et al.

[Title Page](#)[Abstract](#)[Introduction](#)[Conclusions](#)[References](#)[Tables](#)[Figures](#)[◀](#)[▶](#)[◀](#)[▶](#)[Back](#)[Close](#)[Full Screen / Esc](#)[Printer-friendly Version](#)[Interactive Discussion](#)

Appendix A

Backscatter lidar parameter definition

In this appendix, we are aiming at defining the parameters derived from a backscatter lidar and more precisely from the knowledge of the total volume backscatter coefficient at wavelength λ which can be split into the molecular (Rayleigh) and aerosol contribution:

$$\beta_{\lambda}(z) = \beta_{\lambda,m}(z) + \beta_{\lambda,a}(z) \quad (\text{A1})$$

where the subscripts m and a specify, respectively, molecular, and aerosol contributions to the scattering process. A backscatter lidar measures the range corrected lidar signal, $P_{\lambda}(z)$, at range λ , which can be related to $\beta_{\lambda}(z)$ by the following equation:

$$P_{\lambda}(z) = K_{\lambda}(\beta_{\lambda,m}(z) + \beta_{\lambda,a}(z)) \cdot T_{\lambda,m}(z)^2 \cdot T_{\lambda,a}(z)^2 \quad (\text{A2})$$

where K_{λ} the range independent calibration coefficient of the lidar system and T^2 is the two-way transmittance due to any scattering (or absorbing) species along the optical path between the scattering volume at range z and the lidar. The two-way transmittance for any constituent, x , is

$$T_x(z)^2 = \exp(-2\tau_x(z)) = \exp\left(-2 \int_0^z \sigma_x(z') dz'\right) \quad (\text{A3})$$

where $\tau_x(z)$ specifies the optical depth and $\sigma_x(z)$ is the volume extinction coefficient. Molecular contribution can be estimated with a good accuracy using either a density model or meteorological radiosonde data available for the measurement area. When the aerosol contribution is negligible at a range z_0 near the lidar (i.e. where $\tau_x(z_0)$ is small), one can determinate the lidar system constant K from the value of $P(z_0)$. If we divide $P(z)$ by this value and normalize to the Rayleigh contribution, we obtain the

Title Page

Abstract

Introduction

Conclusions

References

Tables

Figures

◀

▶

◀

▶

Back

Close

Full Screen / Esc

Printer-friendly Version

Interactive Discussion

attenuated backscatter ratio, $R(z)$, given by:

$$R = \frac{P}{K \beta_{\lambda,m} \cdot \exp(-2\tau_{\lambda,m})} \approx 1 + \frac{\beta_{\lambda,a}}{\beta_{\lambda,m}} \quad (\text{A4})$$

if $\tau_{\lambda,a}$ remains small (this is the case for this study).

When a linear polarized laser beam is emitted, depolarization related to backscattering in the atmosphere can be measured by a receiving lidar system with an optical selection of the parallel- and cross-polarized signal. The backscatter ratios, R , for perpendicular- and parallel-polarized light are defined as

$$R_{\perp} = 1 + \frac{\beta_{\perp,a}}{\beta_{\perp,m}} \quad R_{\parallel} = 1 + \frac{\beta_{\parallel,a}}{\beta_{\parallel,m}} \quad (\text{A5})$$

and the ratio of the aerosol cross- to parallel-polarized backscatter coefficient is called the linear volume depolarization ratio, δ_a , given by:

$$\delta_a = \frac{\beta_{\perp,a}}{\beta_{\parallel,a}} = \frac{R_{\perp} - 1}{R_{\parallel} - 1} \cdot \delta_m \quad \delta_m = \frac{\beta_{\perp,m}}{\beta_{\parallel,m}} \quad (\text{A6})$$

The Rayleigh depolarization and its wavelength dependency can be found in Bucholtz (1995), e.g. $\delta_m = 0.015$ at 355 nm. Since this ratio depends critically on the absolute accuracy of the backscatter ratio retrieval, the ratio of the total cross- to the total parallel-polarized backscatter coefficient is also used and called hereafter the pseudo depolarization ratio δ given by:

$$\delta = \frac{\beta_{\perp}}{\beta_{\parallel}} = \frac{P_{\perp}}{P_{\parallel}} = \delta_a \left(1 - \frac{1}{R_{\parallel}} \right) + \frac{\delta_m}{R_{\parallel}} \quad (\text{A7})$$

The pseudo depolarization ratio, δ , tends to δ_m only in a clean region where R_{\parallel} tends to 1. Notice that in a thick aerosol layer where the aerosol depolarisation is less than the molecular depolarisation, δ could tend to zero. The pseudo depolarization ratio δ has the advantage of being less unstable when the aerosol layer is weak and it

Title Page

Abstract

Introduction

Conclusions

References

Tables

Figures

◀

▶

◀

▶

Back

Close

Full Screen / Esc

Printer-friendly Version

Interactive Discussion



Airborne measurements of aerosol optical properties

R. Adam de Villiers et al.

Title Page

Abstract

Introduction

Conclusions

References

Tables

Figures

◀

▶

◀

▶

Back

Close

Full Screen / Esc

Printer-friendly Version

Interactive Discussion

is also less dependent on instrumental parameters (Cairo et al., 1999). According to Freudenthaler et al. (2009), the aerosol depolarization ratio δ_a has only a small spectral variation between 532 nm and 355 nm for dust particles, i.e. for aerosol with a large depolarisation value. For example, they found that δ_a is 0.3 at 532 nm and 0.28 at 355 nm for saharan dust plume. However the wavelength dependency of δ is related also to the spectral change of the backscatter ratio. This will have to taken into account when comparing δ_{355} and δ_{532} . For example, the layer II-A discussed in this paper has a δ_a value of the order of 3%, while $R_{355}=1.5$ and $R_{532}=2$. Assuming no spectral variation of δ_a implies a δ variation from 2% to 2.2% when switching the wavelength from 355 to 532 nm.

The ratio of aerosol backscatter at 1064 nm to the aerosol backscatter at 532 nm is called the color ratio, CR, given by

$$\text{CR} = \frac{\beta_{a,1.06}}{\beta_{a,0.53}} = \frac{R_{1.06} - 1}{R_{0.53} - 1} \cdot \frac{1}{16} \quad (\text{A8})$$

where 1/16 is the ratio of the 1064-nm to the 532-nm molecular backscatter. The ratio of total backscatter at 532 nm and the total backscatter at 1064 nm can also be calculated for the same reasons which lead us to use the pseudo depolarization ratio. This new ratio, called hereafter the pseudo color ratio, is related to CR by the following equation:

$$\text{CR}^* = \frac{\beta_{1.06}}{\beta_{0.53}} = \text{CR} \left(1 - \frac{1}{R_{0.53}} \right) + \frac{1}{16R_{0.53}} \quad (\text{A9})$$

The pseudo ratio CR^* can be as small as 1/16, when the aerosol contribution is small (i.e. R much less than 1.5). The CR ratio provides a better representation of the size influence on the aerosol optical properties variation with the wavelength (O'Neill et al., 2003) as it is more directly related to the Angström coefficient which is the standard parameter for discussing this spectral dependency and which is defined as:

$$k = - \frac{d \ln \tau_a}{d \ln \lambda} \quad (\text{A10})$$

Since k depends on aerosol extinction and not on aerosol backscatter coefficients, the relation between k and CR depends on the ratio of these two coefficient, also called the lidar ratio B . The ratio CR is related to k by the equation:

$$CR = \frac{B_{0.5,a}}{B_{1.06,a}} \cdot 2^{-k}. \quad (\text{A11})$$

5 When the fine mode aerosol contribution decreases, k varies from values around 2 to values near 0 and CR increases from values near 0.5 to values near 1, assuming that the corresponding $\frac{B_{0.53,a}}{B_{1.06,a}}$ changes goes from 2 to 1 according to Gattrall et al. (2005). The change of the pseudo ratio CR* goes in the same direction, but with a smaller amplitude as R decreases. For example, CR* does not exceeds 0.5 even for the largest
10 CR values when R remains around 2. Notice also that for small optical depths and small values of the coarse mode fraction, the model calculation of (O'Neill et al., 2003) suggests that k can be larger than 2 and therefore the smallest CR* may become less than 0.2 even when R does not become too small (i.e above 1.5).

15 *Acknowledgements.* The UMS SAFIRE is acknowledged for supporting the ATR-42 aircraft deployment and for providing the aircraft meteorological data. The POLARCAT-FRANCE project was supported by ANR, CNES, CNRS/INSU and IPEV. Ariane Bazureau is acknowledged for her work on FLEXPART modeling. John Burkhart from NILU is acknowledged for providing FLEXPART products on the POLARCAT web site.



The publication of this article is financed by CNRS-INSU.

27814

ACPD

9, 27791–27836, 2009

Airborne measurements of aerosol optical properties

R. Adam de Villiers et al.

Title Page

Abstract

Introduction

Conclusions

References

Tables

Figures

⏪

⏩

◀

▶

Back

Close

Full Screen / Esc

Printer-friendly Version

Interactive Discussion



References

- Atlas, E. L., Ridley, B. A., and Cantrell, C.: The Tropospheric Ozone Production about the Spring Equinox (TOPSE) Experiment: introduction, *J. Geophys. Res.*, 108(D4), 8353, doi:10.1029/2002JD003172, 2003. 27793
- 5 Bethan, S., Vaughan, G., and Reid, S.: A comparison of ozone and thermal tropopause heights and the impact of tropopause definition on quantifying the ozone content of the troposphere, *Q. J. Roy. Meteor. Soc.*, 122, 929–944, 1996. 27803
- Browell, E. V., Hair, J., Butler, C., Grant, W., DeYoung, R., Fenn, M., Brackett, V., Clayton, M., Brasseur, L., Harper, D., Ridley, B., Klonecki, A., Hess, P., Emmons, L., Tie, X., Atlas, E.,
10 Cantrell, C., Wimmers, A., Blake, D., Coffey, M., Hannigan, J., Dibb, J., Talbot, R., Flocke, F., Weinheimer, A., Fried, A., Wert, B., Snow, J., and Lefer, B.: Ozone, aerosol, potential vorticity, and trace gas trends observed at high-latitudes over North America from February to May 2000, *J. Geophys. Res.*, 108(D4), 8369, doi:10.1029/2001JD001390, 2003. 27794
- Bucholtz, A.: Rayleigh-scattering calculations for the terrestrial atmosphere, *Appl. Optics*, 34, 2765–2773, doi:10.1364/AO.34.002765, <http://ao.osa.org/abstract.cfm?URI=ao-34-15-2765>, 1995. 27812
- 15 Cairo, F., Donfrancesco, G. D., Adriani, A., Pulvirenti, L., and Fierli, F.: Comparison of various linear depolarization parameters measured by lidar, *Appl. Optics*, 38, 4425–4432, <http://ao.osa.org/abstract.cfm?URI=ao-38-21-4425>, 1999. 27813
- 20 Catrall, C., Reagan, J., Thome, K., and Dubovik, O.: Variability of aerosol and spectral lidar and backscatter and extinction ratios of key aerosol types derived from selected Aerosol Robotic Network locations, *J. Geophys. Res.*, 110, D10S11, doi:10.1029/2004JD005124, 2005. 27797, 27798, 27807, 27814
- Coheur, P.-F., Clarisse, L., Turquety, S., Hurtmans, D., and Clerbaux, C.: IASI measurements of reactive trace species in biomass burning plumes, *Atmos. Chem. Phys.*, 9, 5655–5667, 2009, <http://www.atmos-chem-phys.net/9/5655/2009/>. 27804
- Duce, R. A., Unni, C. K., Ray, B. J., Prospero, J. M., and Merrill, J. T.: Long-range atmospheric transport of soil dust from Asia to the Tropical North Pacific: temporal variability, *Science*, 209, 1522–1524, <http://www.jstor.org/stable/1684974>, 1980. 27806
- 30 Engvall, A., Krejci, R., Ström, J., Minikin, A., Treffeisen, R., Stohl, A., and Herber, A.: In-situ airborne observations of the microphysical properties of the Arctic tropospheric aerosol during

Airborne measurements of aerosol optical properties

R. Adam de Villiers et al.

Title Page

Abstract

Introduction

Conclusions

References

Tables

Figures

◀

▶

◀

▶

Back

Close

Full Screen / Esc

Printer-friendly Version

Interactive Discussion



late spring and summer, *Tellus B*, 60(3), 392–404, doi:10.1111/j.1600-0889.2008.00348.x, 2008. 27793

Fehsenfeld, F. C., Ancellet, G., Bates, T. S., Goldstein, A. H., Hardesty, R. M., Honrath, R., Law, K. S., Lewis, A. C., Leaitch, R., McKeen, S., Meagher, J., Parrish, D. D., Pszenny, A. A. P., Russell, P. B., Schlager, H., Seinfeld, J., Talbot, R., and Zbinden, R.: International Consortium for Atmospheric Research on Transport and Transformation (ICARTT): North America to Europe overview of the 2004 summer field study, *J. Geophys. Res.*, 111, D23S01, doi:10.1029/2006JD007829, 2006. 27794

Fisher, J. A., Jacob, D. J., Purdy, M. T., Kopacz, M., Le Sager, P., Carouge, C., Holmes, C. D., Yantosca, R. M., Batchelor, R. L., Strong, K., Diskin, G. S., Fuelberg, H. E., Holloway, J. S., Hyer, E. J., McMillan, W. W., Warner, J., Streets, D. G., Zhang, Q., Wang, Y., and Wu, S.: Source attribution and interannual variability of Arctic pollution in spring constrained by aircraft (ARCTAS, ARCPAC) and satellite (AIRS) observations of carbon monoxide, *Atmos. Chem. Phys. Discuss.*, 9, 19035–19080, 2009, <http://www.atmos-chem-phys-discuss.net/9/19035/2009/>. 27807

Freudenthaler, V., Esselborn, M., Wiegner, M., Heese, B., Tesche, M., Ansmann, A., Müller, D., Althausen, D., Wirth, M., Fix, A., Ehret, G., Knippertz, P., Toledano, C., Gasteiger, J., Garhammer, M., and Seefeldner, M.: Depolarization ratio profiling at several wavelengths in pure Saharan dust during SAMUM 2006, *Tellus*, 61B, 165–179, doi:10.1111/j.1600-0889.2008.00396.x, <http://dx.doi.org/10.1111/j.1600-0889.2008.00396.x>, 2009. 27797, 27813

Fuelberg, H. E., Harrigan, D. L., and Sessions, W.: A meteorological overview of the ARCTAS 2008 mission, *Atmos. Chem. Phys. Discuss.*, 9, 18417–18478, 2009, <http://www.atmos-chem-phys-discuss.net/9/18417/2009/>. 27807, 27808

Garrett, T. and Zhao, C.: Increased Arctic cloud longwave emissivity associated with pollution from mid-latitudes, *Nature*, 440, 787–789, 2006. 27793

Gobbi, G. P., Barnaba, F., Van Dingenen, R., Putaud, J. P., Mircea, M., and Facchini, M. C.: Lidar and in situ observations of continental and Saharan aerosol: closure analysis of particles optical and physical properties, *Atmos. Chem. Phys.*, 3, 2161–2172, 2003, <http://www.atmos-chem-phys.net/3/2161/2003/>. 27798

Hamonou, E., Chazette, P., Balis, D., Dulac, F., Schneider, X., Galani, E., Ancellet, G., and Pappayannis, A.: Characterization of the vertical structure of Saharan dust export to the mediterranean basin, *J. Geophys. Res.*, 104, 22257–22270, 1999. 27808

ACPD

9, 27791–27836, 2009

Airborne measurements of aerosol optical properties

R. Adam de Villiers et al.

Title Page

Abstract

Introduction

Conclusions

References

Tables

Figures

◀

▶

◀

▶

Back

Close

Full Screen / Esc

Printer-friendly Version

Interactive Discussion

**Airborne
measurements of
aerosol optical
properties**

R. Adam de Villiers et al.

Title Page

Abstract

Introduction

Conclusions

References

Tables

Figures

◀

▶

◀

▶

Back

Close

Full Screen / Esc

Printer-friendly Version

Interactive Discussion

Jacob, D. J., Crawford, J. H., Maring, H., Clarke, A. D., Dibb, J. E., Ferrare, R. A., Hostetler, C. A., Russell, P. B., Singh, H. B., Thompson, A. M., Shaw, G. E., McCauley, E., Pederson, J. R., and Fisher, J. A.: The ARCTAS aircraft mission: design and execution, *Atmos. Chem. Phys. Discuss.*, 9, 17073–17123, 2009,

<http://www.atmos-chem-phys-discuss.net/9/17073/2009/>. 27794

Law, K. and Stohl, A.: Arctic Air Pollution: Origins and Impacts, *Science*, 315(5818), 1537–1540, doi:10.1126/science.1137695, 2007. 27793

Liu, Z., Vaughan, M., Winker, D., Kittaka, C., Getzewich, B., Kuehn, R., Omar, A., Powell, K., Trepte, C., and Hostetler, C.: The CALIPSO lidar cloud and aerosol discrimination: version 2 algorithm and initial assessment of performance, *J. Atmos. Ocean. Tech.*, 26, 1198–1213, doi:10.1175/2009JTECHA1229.1, 2009. 27805

Methven, J., Arnold, S. R., Stohl, A., Avery, M., Law, K., Lewis, A., Parrish, D., Reeves, C., Schlager, H., Atlas, E., Blake, D., and Rappenglück, B.: Establishing Lagrangian connections between observations within air masses crossing the Atlantic during the ICARTT experiment, *J. Geophys. Res.*, 111, D23S62, doi:10.1029/2006JD007540, 2006. 27801

Omar, A., Winker, D., Kittaka, C., Vaughan, M., Liu, Z., Hu, Y., Trepte, C., Rogers, R., Ferrare, R., Lee, K., Kuehn, R., and Hostetler, C.: The CALIPSO automated aerosol classification and lidar ratio selection algorithm, *J. Atmos. Ocean. Tech.*, 26, 1994–2014, doi:10.1175/2009JTECHA1231.1, 2009. 27805

O'Neill, N., Eck, T., Smirnov, A., Holben, B., and Thulasiraman, S.: Spectral discrimination of coarse and fine mode optical depth, *J. Geophys. Res.*, 108, 4559, doi:10.1029/2002JD002975, 2003. 27813, 27814

Paris, J.-D., Arshinov, M. Y., Ciais, P., Belan, B. D., and Nédélec, P.: Large-scale aircraft observations of ultra-fine and fine particle concentrations in the remote Siberian troposphere: new particle formation studies, *Atmos. Environ.*, 43, 1302–1309, doi:10.1016/j.atmosenv.2008.11.032, <https://access-distant.upmc.fr:443/http://www.sciencedirect.com/science/article/B6VH3-4V35470-5/2/1fb175cceb8cd16d86d47a1c8ca60cf0>, 2009. 27807

Pueschel, R. and Kinne, S.: Physical and radiative properties of Arctic atmospheric aerosols, *Sci. Total Environ.*, 160–161, 811–824, doi:10.1016/0048-9697(95)04414-V, 1995. 27793

Quinn, P. K., Bates, T. S., Baum, E., Doubleday, N., Fiore, A. M., Flanner, M., Fridlind, A., Garrett, T. J., Koch, D., Menon, S., Shindell, D., Stohl, A., and Warren, S. G.: Short-lived pollutants in the Arctic: their climate impact and possible mitigation strategies, *Atmos. Chem. Phys.*, 8, 1723–1735, 2008,

**Airborne
measurements of
aerosol optical
properties**

R. Adam de Villiers et al.

[Title Page](#)[Abstract](#)[Introduction](#)[Conclusions](#)[References](#)[Tables](#)[Figures](#)[⏪](#)[⏩](#)[◀](#)[▶](#)[Back](#)[Close](#)[Full Screen / Esc](#)[Printer-friendly Version](#)[Interactive Discussion](#)

<http://www.atmos-chem-phys.net/8/1723/2008/>. 27793

Rahn, K. A.: Relative importances of North America and Eurasia as sources of arctic aerosol, *Atmos. Environ.*, 15, 1447–1455, doi:10.1016/0004-6981(81)90351-6, 1981. 27793

Scheuer, E., Talbot, R. W., Dibb, J. E., Seid, G. K., DeBell, L., and Lefer, B.: Seasonal distributions of fine aerosol sulfate in the North American Arctic basin during TOPSE, *J. Geophys. Res.*, 108(D4), 8370, doi:10.1029/2001JD001364, 2003. 27794

Seibert, P. and Frank, A.: Source-receptor matrix calculation with a Lagrangian particle dispersion model in backward mode, *Atmos. Chem. Phys.*, 4, 51–63, 2004, <http://www.atmos-chem-phys.net/4/51/2004/>. 27803

Sellegrì, K., Hanke, M., Umann, B., Arnold, F., and Kulmala, M.: Measurements of organic gases during aerosol formation events in the boreal forest atmosphere during QUEST, *Atmos. Chem. Phys.*, 5, 373–384, 2005, <http://www.atmos-chem-phys.net/5/373/2005/>. 27800

Shindell, D. T., Chin, M., Dentener, F., Doherty, R. M., Faluvegi, G., Fiore, A. M., Hess, P., Koch, D. M., MacKenzie, I. A., Sanderson, M. G., Schultz, M. G., Schulz, M., Stevenson, D. S., Teich, H., Textor, C., Wild, O., Bergmann, D. J., Bey, I., Bian, H., Cuvelier, C., Duncan, B. N., Folberth, G., Horowitz, L. W., Jonson, J., Kaminski, J. W., Marmer, E., Park, R., Pringle, K. J., Schroeder, S., Szopa, S., Takemura, T., Zeng, G., Keating, T. J., and Zuber, A.: A multi-model assessment of pollution transport to the Arctic, *Atmos. Chem. Phys.*, 8, 5353–5372, 2008, <http://www.atmos-chem-phys.net/8/5353/2008/>. 27793

Stohl, A., Hittenberger, M., and Wotawa, G.: Validation of the Lagrangian particle dispersion model FLEXPART against large scale tracer experiment data, *Atmos. Environ.*, 32, 4245–4264, 1998. 27801

Stohl, A., Eckhardt, S., Forster, C., James, P., Spichtinger, N., and Seibert, P.: A replacement for simple back trajectory calculations in the interpretation of atmospheric trace substance measurements, *Atmos. Environ.*, 36, 4635–4648, 2002. 27801

Stohl, A., Cooper, O. R., Damoah, R., Fehsenfeld, F. C., Forster, C., Hsie, E. Y., Hübler, G., Parrish, D. D., and Trainer, M.: Forecasting for a Lagrangian aircraft campaign, *Atmos. Environ.*, 4, 2405–2433, 2004. 27795

Stohl, A., Berg, T., Burkhardt, J. F., Fjæraa, A. M., Forster, C., Herber, A., Hov, Ø., Lunder, C., McMillan, W. W., Oltmans, S., Shiobara, M., Simpson, D., Solberg, S., Stebel, K., Ström, J., Tørseth, K., Treffeisen, R., Virkkunen, K., and Yttri, K. E.: Arctic smoke - record high air

pollution levels in the European Arctic due to agricultural fires in Eastern Europe in spring 2006, *Atmos. Chem. Phys.*, 7, 511–534, 2007,

<http://www.atmos-chem-phys.net/7/511/2007/>. 27793

5 Stohl, A., Forster, C., Huntrieser, H., Mannstein, H., McMillan, W. W., Petzold, A., Schlager, H., and Weinzierl, B.: Aircraft measurements over Europe of an air pollution plume from Southeast Asia - aerosol and chemical characterization, *Atmos. Chem. Phys.*, 7, 913–937, 2007,

<http://www.atmos-chem-phys.net/7/913/2007/>. 27794

10 Streets, D. and Waldhoff, S.: Present and future emissions of air pollutants in China: SO₂, NO_x, and CO, *Atmos. Environ.*, 34, 363–374, doi:10.1016/S1352-2310(99)00167-3, <http://www.sciencedirect.com/science/article/B6VH3-3Y162CG-3/2/dfaeb3ef6e2170f1b0e299716e58ee1f>, 2000. 27803

15 Sugimoto, N. and Lee, C. H.: Characteristics of dust aerosols inferred from lidar depolarization measurements at two wavelengths, *Appl. Optics.*, 45, 7468–7474, <http://ao.osa.org/abstract.cfm?URI=ao-45-28-7468>, 2006. 27797

20 Warneke, C., Bahreini, R., Brioude, J., Brock, C., de Gouw, J., Fahey, D., Froyd, K., Holloway, J., Middlebrook, A., Miller, L., Montzka, S., Murphy, D., Peischl, J., Ryerson, T., Schwarz, J., Spackman, J., and Veres, P.: Biomass burning in Siberia and Kazakhstan as an important source for haze over the Alaskan Arctic in April 2008, *Geophys. Res. Lett.*, 36, L02813, doi:10.1029/2008GL036194, 2009. 27804

25 Weber, R., Orsini, D., Wang, B., Scheuer, E., Talbot, R., Dibb, J., Seid, G., DeBell, L., Mauldin, R., Kosciuch, E., Cantrell, C., and Eisele, F.: Investigations into free tropospheric new particle formation in the central Canadian arctic during the winter/spring transition as part of TOPSE, *J. Geophys. Res.*, 108(D4), 8357, doi:10.1029/2002JD002239, 2003. 27794, 27800

ACPD

9, 27791–27836, 2009

**Airborne
measurements of
aerosol optical
properties**

R. Adam de Villiers et al.

Title Page

Abstract

Introduction

Conclusions

References

Tables

Figures

⏪

⏩

◀

▶

Back

Close

Full Screen / Esc

Printer-friendly Version

Interactive Discussion

**Airborne
measurements of
aerosol optical
properties**

R. Adam de Villiers et al.

Table 1. Airborne Lidar data characteristics.

Wavelengths:	355, 532, 1064 nm
Perpendicular depolarisation:	355 nm
Horizontal resolution:	100 m
Horizontal resolution for aerosol analysis:	2 km
Vertical resolution:	7 m
Vertical resolution for aerosol analysis:	30 m

[Title Page](#)[Abstract](#)[Introduction](#)[Conclusions](#)[References](#)[Tables](#)[Figures](#)[I◀](#)[▶I](#)[◀](#)[▶](#)[Back](#)[Close](#)[Full Screen / Esc](#)[Printer-friendly Version](#)[Interactive Discussion](#)

Airborne measurements of aerosol optical properties

R. Adam de Villiers et al.

Table 2. Aerosol layer characteristics from the airborne lidar observations.

Lidar layer	Layer latitude	Altitude range, km	Aerosol color ratio	Pseudo color ratio	δ_{355}
I	68.9° N	3.5–5	0.21±0.11	$9\pm 1.1\times 10^{-2}$	1.3±0.3%
II-A	69.6° N	2.8–3.8	0.2±0.02	$13\pm 0.9\times 10^{-2}$	1.9±0.2%
PBL	70.6° N	<0.8	0.22±0.07	$9\pm 1.1\times 10^{-2}$	1.7±0.25%
II-B	71.7° N	3.5–4.5	0.28±0.08	$10\pm 1.0\times 10^{-2}$	1.3±0.3%

Title Page

Abstract

Introduction

Conclusions

References

Tables

Figures

◀

▶

◀

▶

Back

Close

Full Screen / Esc

Printer-friendly Version

Interactive Discussion

Table 3. Aerosol layer characteristics from the CALIPSO observations for the backward FLEX-PART model run initialized at 69.5° N–72.5° N, 3.5–4.5 km (Layer II-A and II-B).

**Airborne
measurements of
aerosol optical
properties**

R. Adam de Villiers et al.

Title Page

Abstract

Introduction

Conclusions

References

Tables

Figures

◀

▶

◀

▶

Back

Close

Full Screen / Esc

Printer-friendly Version

Interactive Discussion



CALIOP Date	CALIOP Time UT	CALIOP start Lat./Lon.	CALIOP end Lat./Lon.	Flexpart layer alt., km	Mean β_{532} in $\text{km}^{-1}\text{sr}^{-1}$	Color ratio	Mean δ_{532}
05/04	03:21–04:14	51.38/135.81	52.39/135.35	5.2–7.2	$22\pm 4\times 10^{-4}$	0.36±0.16	0.12±0.17
05/04	05:00–05:52	51.73/110.94	52.38/110.63	2.2–4.2	$18\pm 3\times 10^{-4}$	0.33±0.16	0.10±0.11
05/04	12:28–13:15	61.81/–146.33	63.65/–144.88	2.1–4.1	$39\pm 22\times 10^{-4}$	0.38±0.45	0.11±0.15
05/04	17:25–18:11	42.55/130.16	47.77/132.06	1–2.2	$39\pm 12\times 10^{-4}$	0.39±0.18	0.07±0.06
05/04	19:04–19:50	56.34/111.3	61.41/114.49	3.7–5.7	$14\pm 3\times 10^{-4}$	0.27±0.19	0.04±0.04
05/04	20:43–21:29	56.26/86.54	57.09/87	3.2–5.2	$16\pm 3\times 10^{-4}$	0.3±0.14	0.06±0.04
05/04	22:21–23:08	59.06/63.46	62.42/65.8	5.3–7.3	$12\pm 2\times 10^{-4}$	0.32±0.15	0.09±0.05
05/04	22:21–23:08	68.55/71.74	69.83/73.41	5.5–7.5	$13\pm 3\times 10^{-4}$	0.26±0.17	0.11±0.06
06/04	04:05–04:57	50.26/125.48	51.4/124.98	1.5–3.5	$25\pm 3\times 10^{-4}$	0.33±0.16	0.06±0.11
06/04	07:22–08:15	56.41/73.06	57.06/72.7	5–7	$15\pm 2\times 10^{-4}$	0.3±0.17	0.11±0.11
06/04	13:12–13:58	65.12/–154.4	67.1/–152.42	3.7–6.5	$15\pm 5\times 10^{-4}$	0.05±0.4	0.07±0.07
06/04	14:50–15:37	65.59/–178.68	65.72/–178.56	4.8–6.8	$15\pm 3\times 10^{-4}$	0.53±0.35	0.10±0.08
06/04	19:47–20:33	57.97/101.42	58.62/101.81	4.7–6.7	$10\pm 1\times 10^{-4}$	0.13±0.1	0.04±0.02
06/04	23:51–00:44	58.61/–175.44	59.43/–175.96	4.9–6.9	$21\pm 4\times 10^{-4}$	0.22±0.18	0.09±0.11
07/04	03:09–04:01	47.42/140.54	50.5/139.28	1–3.4	$40\pm 12\times 10^{-4}$	0.55±0.18	0.13±0.18
07/04	03:09–04:01	50.81/139.14	51.78/138.71	1–2.8	$35\pm 12\times 10^{-4}$	1.02±0.61	0.11±0.17
07/04	04:48–05:40	52.78/113.53	53.26/113.3	2.7–4.7	$32\pm 7\times 10^{-4}$	0.33±0.14	0.00±0.08
07/04	16:20–17:13	72.81/155.56	73.83/157.66	4.7–7	$13\pm 2\times 10^{-4}$	0.27±0.13	0.02±0.02
07/04	17:13–17:59	52.04/136.95	56.15/139.01	1–3.3	$27\pm 6\times 10^{-4}$	0.31±0.25	0.04±0.03
07/04	17:13–17:59	59.11/140.74	64.18/144.49	1–3.4	$27\pm 8\times 10^{-4}$	0.31±0.15	0.02±0.03
07/04	17:59–18:52	75.09/136.02	76.98/141.93	5–7.3	$13\pm 2\times 10^{-4}$	0.27±0.14	0.03±0.04
07/04	18:52–19:38	58.94/115.92	59.59/116.33	5–7	$11\pm 1\times 10^{-4}$	0.24±0.13	0.07±0.04
08/04	00:35–01:27	76.26/150	76.8/148.18	5–7.4	$17\pm 4\times 10^{-4}$	0.27±0.2	0.16±0.11
08/04	02:14–03:06	61.95/146.76	63.27/145.72	1–3	$25\pm 4\times 10^{-4}$	0.3±0.1	0.04±0.11
08/04	17:56–18:43	59.82/130.39	64.89/134.3	2.1–6.6	$17\pm 3\times 10^{-4}$	0.25±0.14	0.04±0.03
08/04	20:21–21:14	80.38/126.27	80.71/129.88	4.8–7.4	$13\pm 2\times 10^{-4}$	0.28±0.13	0.00±0.08
08/04	22:00–22:53	81.3/113.75	81.52/118.4	4.8–7.4	$15\pm 2\times 10^{-4}$	0.3±0.14	0.03±0.09
09/04	02:57–03:49	67.82/130.51	68.44/129.77	4–6.9	$21\pm 5\times 10^{-4}$	0.5±0.19	0.08±0.20
09/04	17:47–18:39	71.9/132.25	75.98/141.63	3.8–5.8	$21\pm 6\times 10^{-4}$	0.29±0.12	0.03±0.03
09/04	19:26–20:18	78.32/126.06	80.65/143.1	3–6.3	$16\pm 2\times 10^{-4}$	0.32±0.12	0.03±0.07
09/04	21:05–21:57	80.89/121.22	81.16/125.21	4.1–6.1	$14\pm 2\times 10^{-4}$	0.35±0.18	0.00±0.06
10/04	02:02–02:54	77.56/23.72	79.66/35.26	4.6–7.4	$14\pm 2\times 10^{-4}$	0.26±0.15	0.03±0.07
10/04	03:40–04:33	81.71/39.83	81.81/47.08	3.7–7.4	$20\pm 4\times 10^{-4}$	0.68±0.36	0.03±0.12
10/04	05:19–06:12	81.8/20.22	81.82/24.04	3.7–6.7	$17\pm 2\times 10^{-4}$	0.15±0.09	0.03±0.09
10/04	06:58–07:51	81.32/19.38	81.68/10.17	3.7–7.4	$15\pm 2\times 10^{-4}$	0.25±0.17	0.05±0.11
11/04	02:45–03:37	73.66/1.25	75.67/6.29	3–5.6	$16\pm 2\times 10^{-4}$	0.27±0.12	0.02±0.03

Airborne measurements of aerosol optical properties

R. Adam de Villiers et al.

Table 4. Aerosol layer characteristics from the CALIPSO observations for the backward FLEX-PART model run initialized at 68.5° N–69° N, 3.5–5 km (Layer I).

Date	CALIOP Time UT	CALIOP start Lat./Lon.	CALIOP end Lat./Lon.	Flexpart layer alt., km	Mean β_{532} in $\text{km}^{-1} \text{sr}^{-1}$	Color ratio	Mean δ_{532}
08/4	01:27–02:14	52.05/13.36	55.86/15.24	1.7–5.4	$27 \pm 1 \times 10^{-4}$	0.44 ± 0.28	0.08 ± 0.06
09/4	02:11–02:57	58.45/5.91	62.72/8.87	3.1–5.3	$17 \pm 4 \times 10^{-4}$	0.23 ± 0.21	0.05 ± 0.06
10/4	02:54–03:40	66.26/1.21	70.21/5.97	2.5–5.3	$16 \pm 4 \times 10^{-4}$	0.23 ± 0.18	0.04 ± 0.03
10/4	10:16–11:08	64.76/23.94	64.88/23.82	2.6–5.0	$39 \pm 13 \times 10^{-4}$	0.40 ± 0.50	0.10 ± 0.14
11/4	01:58–02:45	65.94/14.79	68.41/17.49	2.7–5.2	$16 \pm 3 \times 10^{-4}$	0.10 ± 0.17	0.03 ± 0.02

Title Page

Abstract

Introduction

Conclusions

References

Tables

Figures

⏪

⏩

◀

▶

Back

Close

Full Screen / Esc

Printer-friendly Version

Interactive Discussion

Airborne
measurements of
aerosol optical
properties

R. Adam de Villiers et al.

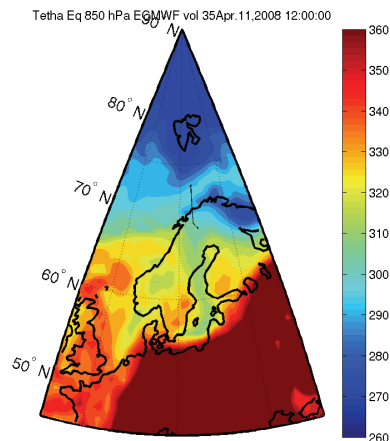
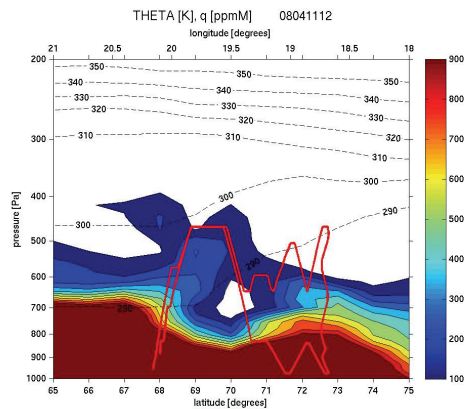


Fig. 1. Vertical cross section of ECMWF specific humidity and potential temperature (top panel) and ECMWF equivalent potential temperature at 850 hPa (bottom panel) for the 11 April 2008 at 12:00 UT. The flight vertical pattern is shown in red.

[Title Page](#)[Abstract](#)[Introduction](#)[Conclusions](#)[References](#)[Tables](#)[Figures](#)[◀](#)[▶](#)[◀](#)[▶](#)[Back](#)[Close](#)[Full Screen / Esc](#)[Printer-friendly Version](#)[Interactive Discussion](#)

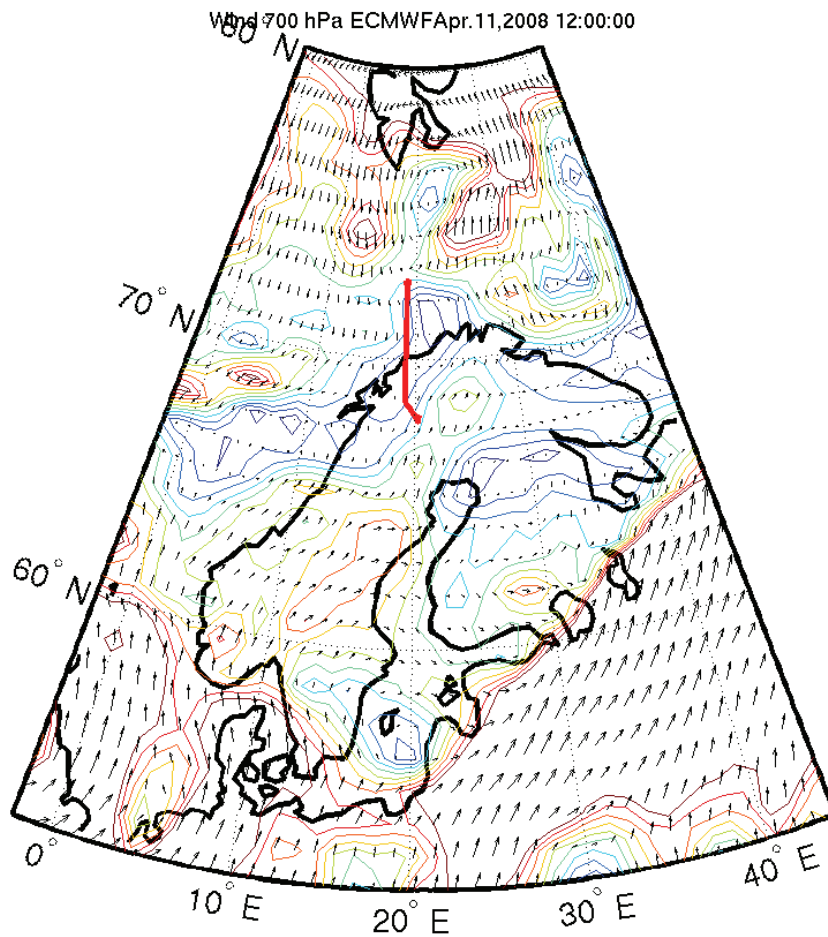


Fig. 2. ECMWF wind field at 700 hPa on 11 April 2008 at 12:00 UT. (Horizontal flight pattern in red.)

**Airborne
measurements of
aerosol optical
properties**

R. Adam de Villiers et al.

Title Page

Abstract

Introduction

Conclusions

References

Tables

Figures

◀

▶

◀

▶

Back

Close

Full Screen / Esc

Printer-friendly Version

Interactive Discussion

**Airborne
measurements of
aerosol optical
properties**

R. Adam de Villiers et al.

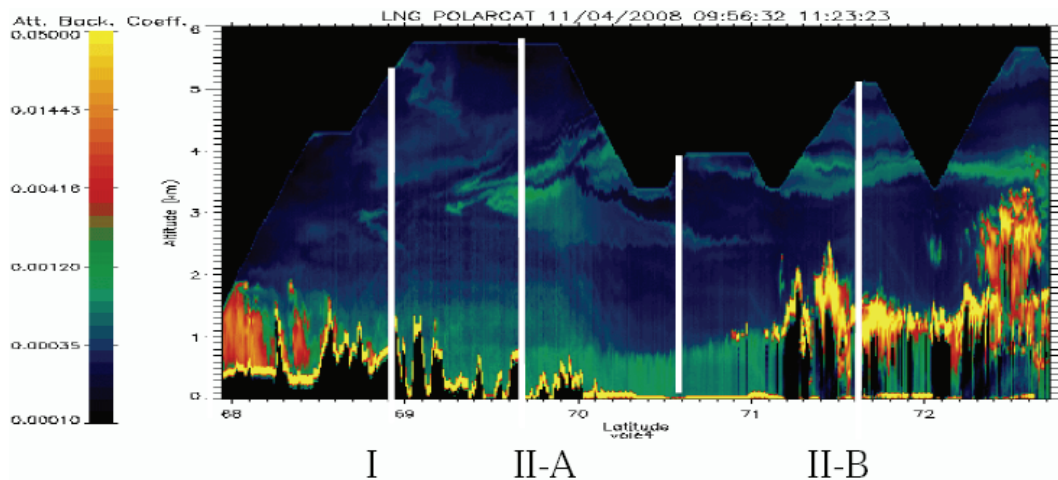


Fig. 3. Vertical cross section of the attenuated backscatter for the 1064 nm channel between 68° N and 72.5° N.

[Title Page](#)[Abstract](#)[Introduction](#)[Conclusions](#)[References](#)[Tables](#)[Figures](#)[⏪](#)[⏩](#)[◀](#)[▶](#)[Back](#)[Close](#)[Full Screen / Esc](#)[Printer-friendly Version](#)[Interactive Discussion](#)

Airborne
measurements of
aerosol optical
properties

R. Adam de Villiers et al.

Title Page

Abstract

Introduction

Conclusions

References

Tables

Figures

◀

▶

◀

▶

Back

Close

Full Screen / Esc

Printer-friendly Version

Interactive Discussion

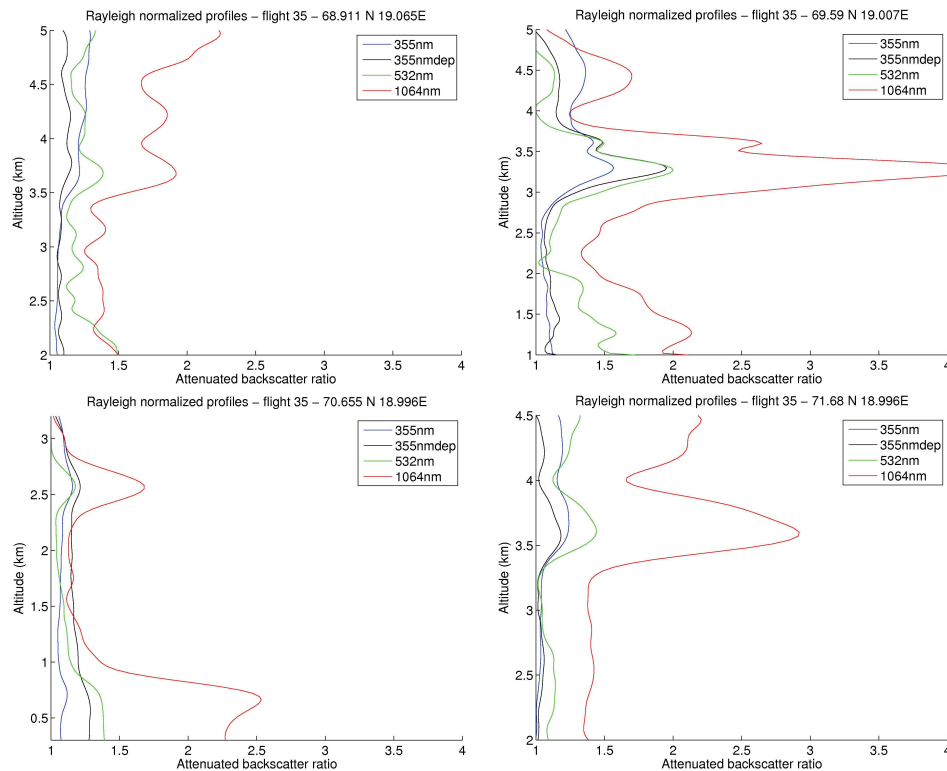


Fig. 4. Lidar vertical profiles of the 20-s averages of the attenuated backscatter ratio at 355, 355 depolarized, 532 and 1064 nm for the 4 layers listed in Table 1.

Airborne
measurements of
aerosol optical
properties

R. Adam de Villiers et al.

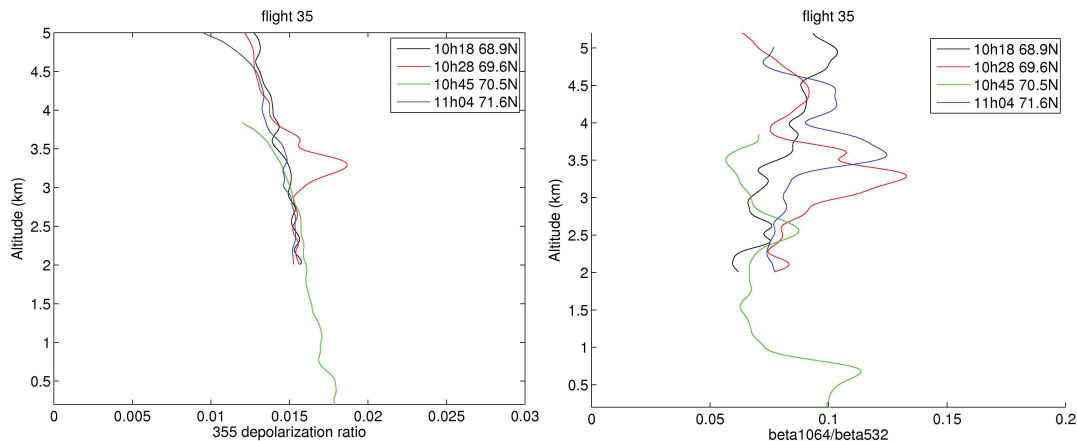


Fig. 5. Vertical profiles of the 355 nm pseudo depolarization ratio δ_{355} and the pseudo color ratio for the layers listed in Table 1.

[Title Page](#)[Abstract](#)[Introduction](#)[Conclusions](#)[References](#)[Tables](#)[Figures](#)[⏪](#)[⏩](#)[◀](#)[▶](#)[Back](#)[Close](#)[Full Screen / Esc](#)[Printer-friendly Version](#)[Interactive Discussion](#)

**Airborne
measurements of
aerosol optical
properties**

R. Adam de Villiers et al.

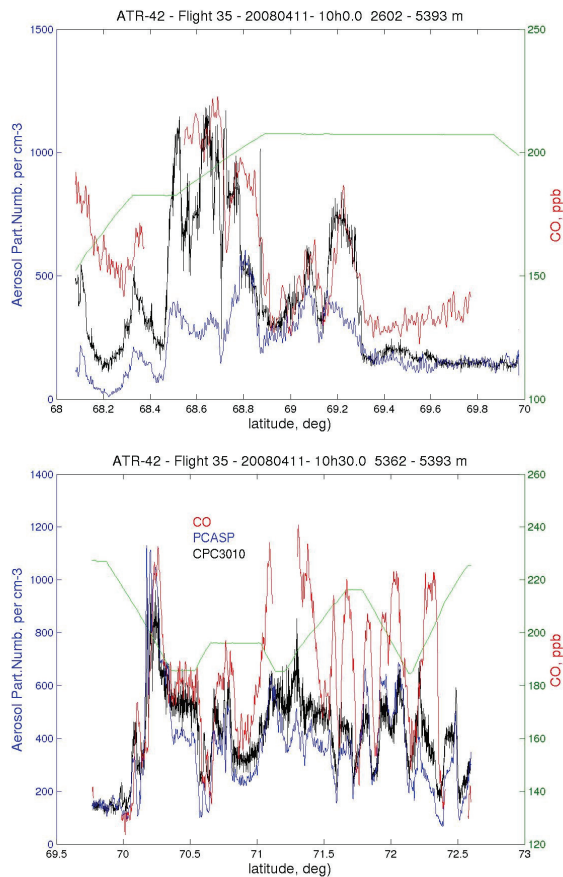


Fig. 6. CO and aerosol concentrations for the PCASP and CPC along the flight track for latitudes $<70^{\circ}\text{N}$ (top panel) and latitudes $>70^{\circ}\text{N}$ (bottom panel).

[Title Page](#)[Abstract](#)[Introduction](#)[Conclusions](#)[References](#)[Tables](#)[Figures](#)[◀](#)[▶](#)[◀](#)[▶](#)[Back](#)[Close](#)[Full Screen / Esc](#)[Printer-friendly Version](#)[Interactive Discussion](#)

**Airborne
measurements of
aerosol optical
properties**

R. Adam de Villiers et al.

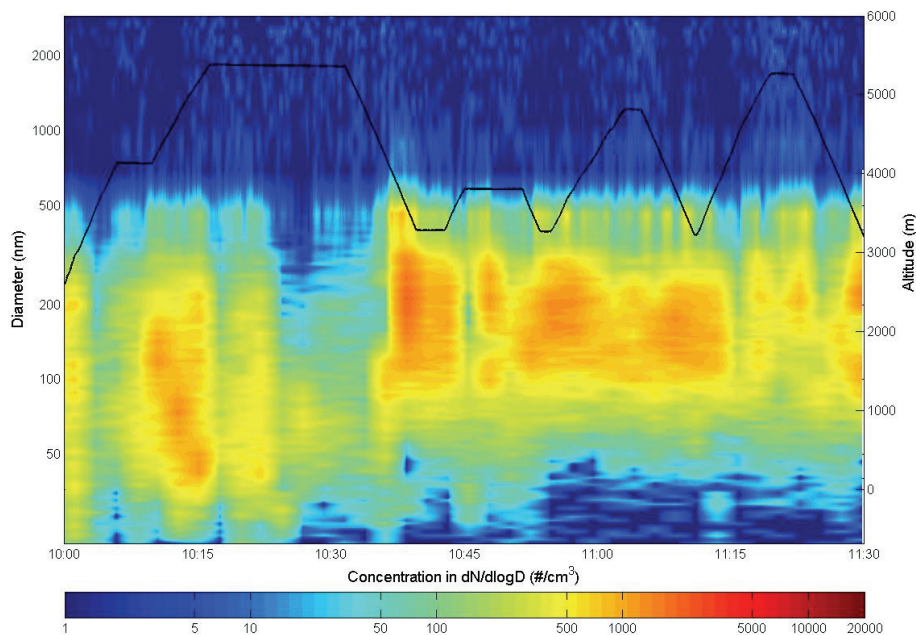


Fig. 7. Size spectrum (nm) measured as a function of time along the flight track by the SMPS (0.01 and 0.4 μm) and PCASP (0.4–3 μm). The black line is the vertical flight pattern.

[Title Page](#)[Abstract](#)[Introduction](#)[Conclusions](#)[References](#)[Tables](#)[Figures](#)[⏪](#)[⏩](#)[◀](#)[▶](#)[Back](#)[Close](#)[Full Screen / Esc](#)[Printer-friendly Version](#)[Interactive Discussion](#)

**Airborne
measurements of
aerosol optical
properties**

R. Adam de Villiers et al.

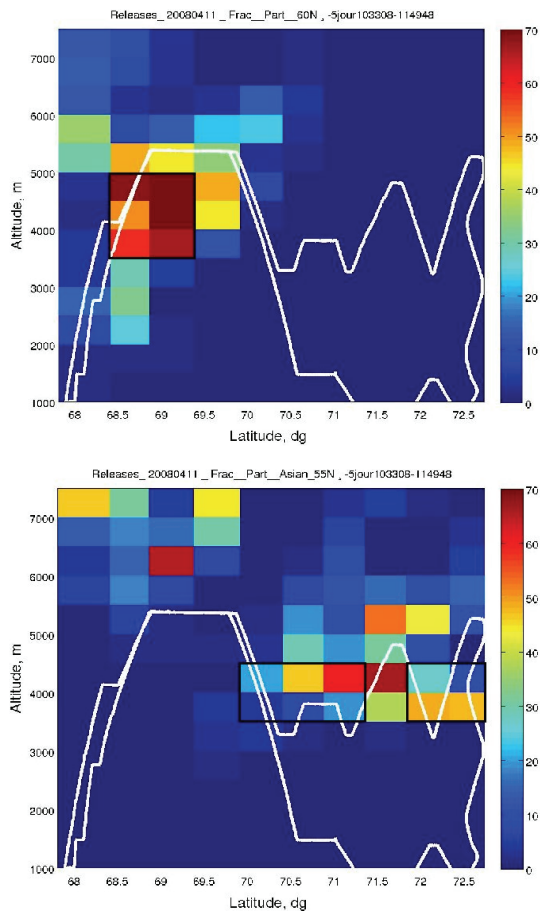


Fig. 8. Meridional vertical cross section of air mass origins calculate by Flexpart for $500\text{ m} \times 0.5^\circ \times 0.5^\circ$ boxes. The color scale indicates the fraction of particles being in the European (first figure) and Asian (second figure) lower troposphere ($z < 3\text{ km}$), 5 days before the observations.

[Title Page](#)[Abstract](#)[Introduction](#)[Conclusions](#)[References](#)[Tables](#)[Figures](#)[◀](#)[▶](#)[◀](#)[▶](#)[Back](#)[Close](#)[Full Screen / Esc](#)[Printer-friendly Version](#)[Interactive Discussion](#)

Airborne
measurements of
aerosol optical
properties

R. Adam de Villiers et al.

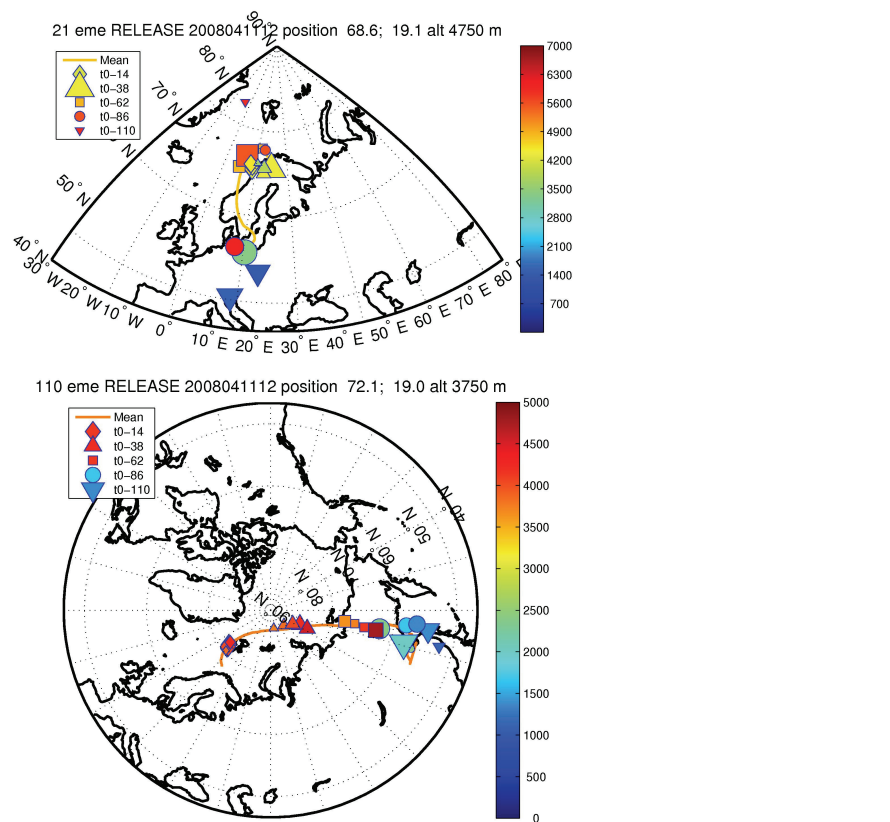


Fig. 9. 5-days FLEXPART backward time position of five clusters of the 2000 particles released between 4 and 4.5 km at 68.6°N (top panel) and between 3.5 and 4 km at 72.1°N (bottom panel) on 11 April 2008 at 12:00 UT. The clusters are plotted every 24 h from 14 h before observation, the color corresponds to their altitude, and the size of each cluster is proportional to the number of particles.

Title Page

Abstract

Introduction

Conclusions

References

Tables

Figures

◀

▶

◀

▶

Back

Close

Full Screen / Esc

Printer-friendly Version

Interactive Discussion

**Airborne
measurements of
aerosol optical
properties**

R. Adam de Villiers et al.

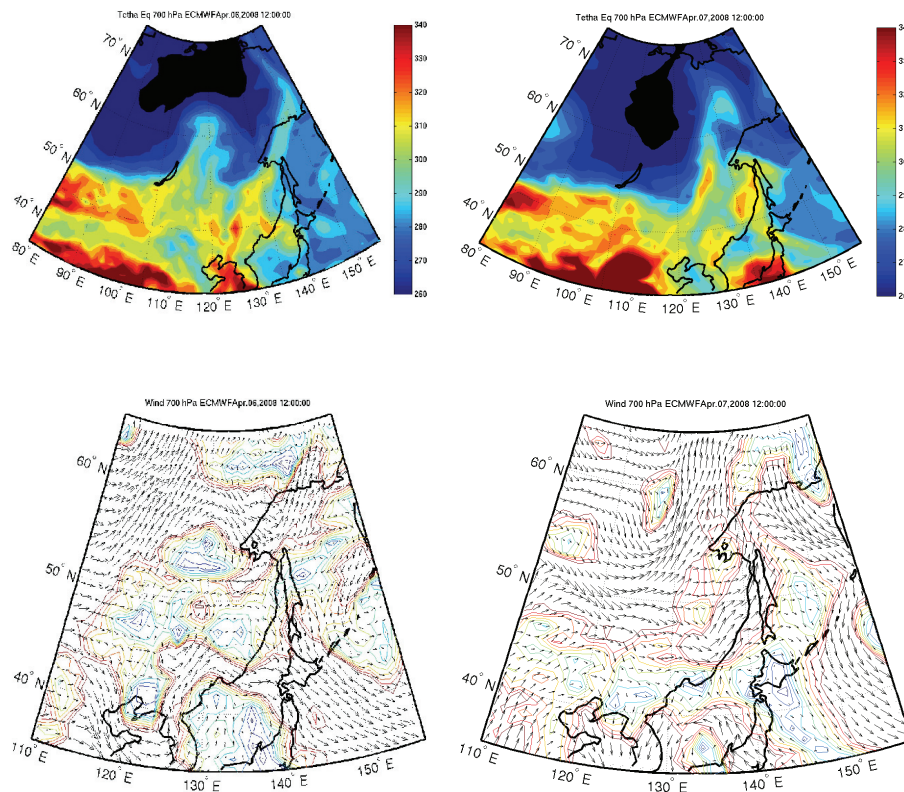


Fig. 10. ECMWF 700 hPa equivalent potential temperature (top row) and ECMWF 700 hPa wind field (bottom row) for the 11 June 2008 (left column) and 11 July 2008 (right column) at 12:00 UT.

[Title Page](#)[Abstract](#)[Introduction](#)[Conclusions](#)[References](#)[Tables](#)[Figures](#)[◀](#)[▶](#)[◀](#)[▶](#)[Back](#)[Close](#)[Full Screen / Esc](#)[Printer-friendly Version](#)[Interactive Discussion](#)

Airborne measurements of aerosol optical properties

R. Adam de Villiers et al.

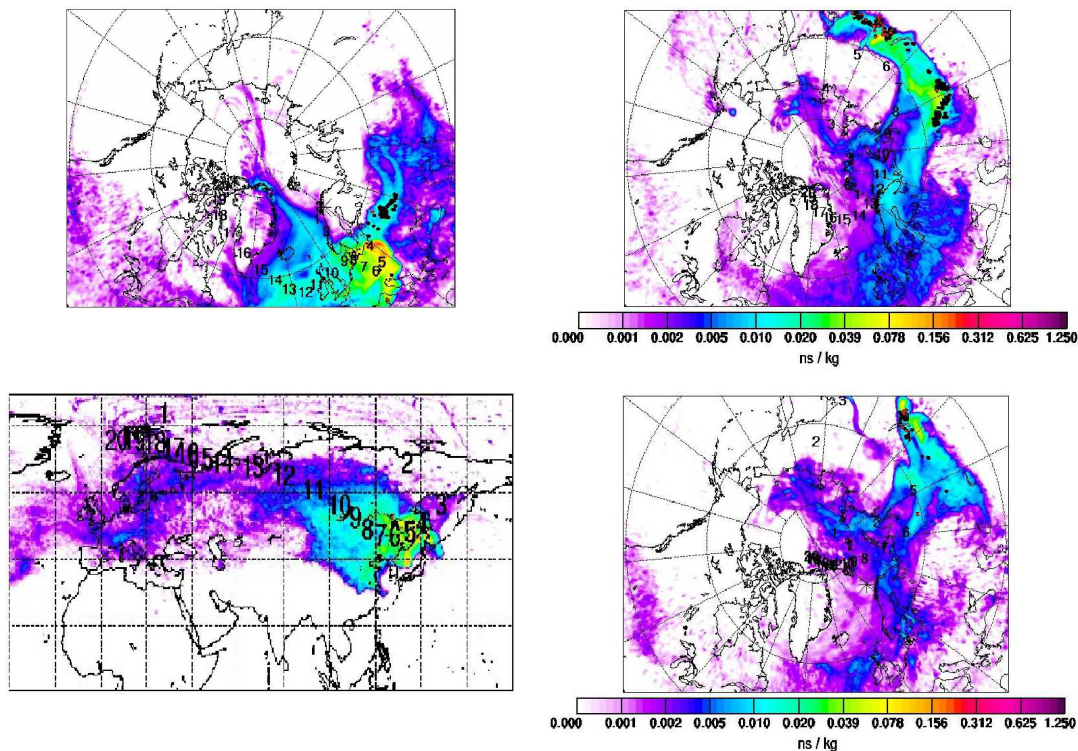


Fig. 11. Potential Emission Sensitivity (PES) in ns/kg for 4 points of the flight track 68.8° N-4500 m, 70.2° N-4200 m, 72° N-3600 m and 72.4° N-5250 m. Numbers indicate elapsed time in days since emission along the mean trajectory. (see http://transport.nilu.no/flexpart-projects?cmp=POLARCAT_FRANCE).

Title Page

Abstract

Introduction

Conclusions

References

Tables

Figures

◀

▶

◀

▶

Back

Close

Full Screen / Esc

Printer-friendly Version

Interactive Discussion

**Airborne
measurements of
aerosol optical
properties**R. Adam de Villiers et al.

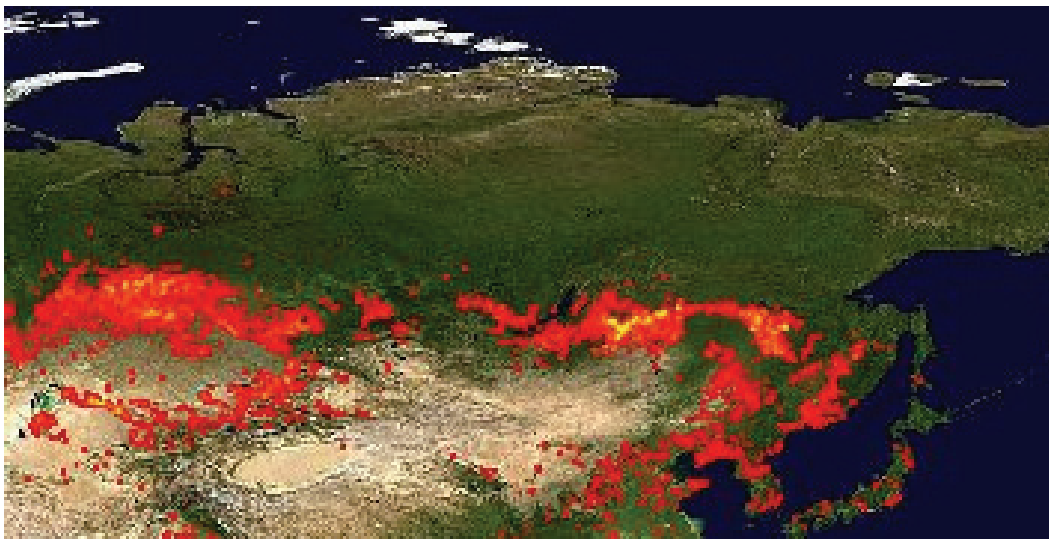


Fig. 12. Fires detected by MODIS over a 10-day period 31 March 2008 to 9 April 2008. Each colored dot indicates a location with at least one fire during the compositing period. Color ranges from low (red) to high (yellow) fire counts.

[Title Page](#)[Abstract](#)[Introduction](#)[Conclusions](#)[References](#)[Tables](#)[Figures](#)[I◀](#)[▶I](#)[◀](#)[▶](#)[Back](#)[Close](#)[Full Screen / Esc](#)[Printer-friendly Version](#)[Interactive Discussion](#)

Airborne measurements of aerosol optical properties

R. Adam de Villiers et al.

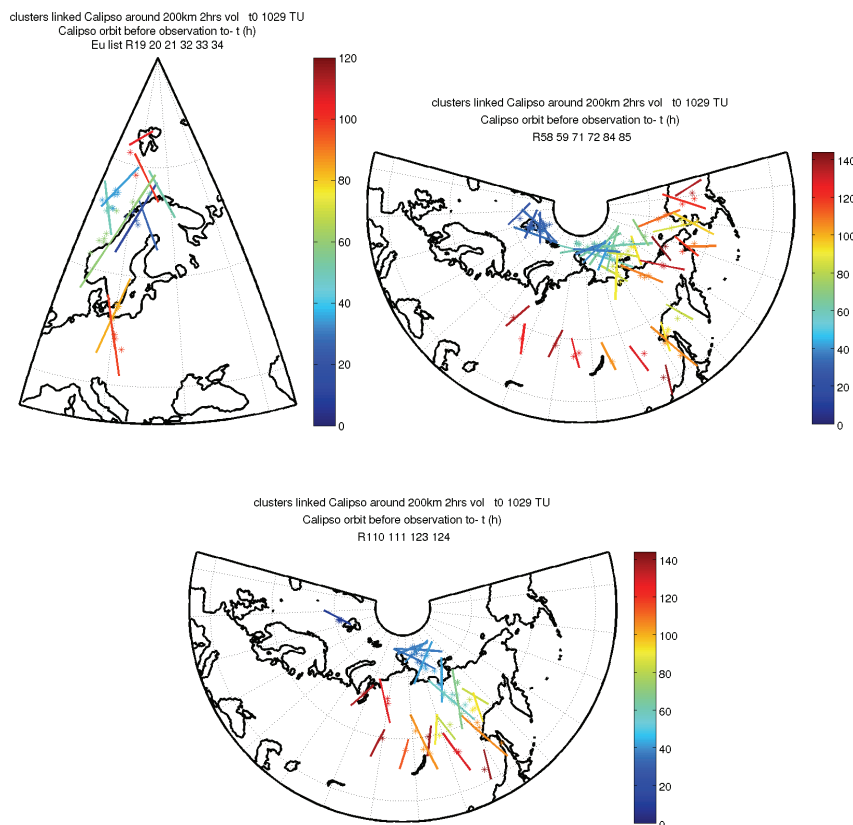


Fig. 13. Calipso track sections (line) and FLEXPART air mass positions (*) along FLEXPART trajectories initialized in the black rectangles of Fig. 8 (top left panel for 69.5° N, top right and bottom panel for, respectively the 70.5° N and 72° N rectangles). The colors scale indicates the elapsed time in hour between the CALIPSO observation and the aircraft observation.

Title Page

Abstract

Introduction

Conclusions

References

Tables

Figures

◀

▶

◀

▶

Back

Close

Full Screen / Esc

Printer-friendly Version

Interactive Discussion